DNA topology dictates emergent bulk elasticity and hindered macromolecular diffusion in DNA-dextran composites

Pawan Khanal, Karthik R. Peddireddy, Juexin Marfai, et al.

Citation: Journal of Rheology **66**, 699 (2022); doi: 10.1122/8.0000447
View online: https://doi.org/10.1122/8.0000447
View Table of Contents: https://sor.scitation.org/toc/jor/66/4
Published by the The Society of Rheology

DNA topology dictates emergent bulk elasticity and hindered macromolecular diffusion in DNA-dextran composites

Pawan Khanal, Karthik R. Peddireddy, Juexin Marfai, Ryan McGorty, and Rae M. Robertson-Anderson[a)]

Department of Physics and Biophysics, University of San Diego, 5998 Alcala Park, San Diego, California 92110

(Received 26 January 2022; final revision received 11 April 2022; published 3 June 2022)

Abstract

Polymer architecture plays critical roles in both bulk rheological properties and microscale macromolecular dynamics in entangled polymer solutions and composites. Ring polymers, in particular, have been the topic of much debate due to the inability of the celebrated reptation model to capture their observed dynamics. Macrorheology and differential dynamic microscopy (DDM) are powerful methods to determine entangled polymer dynamics across scales; yet, they typically require different samples under different conditions, preventing direct coupling of bulk rheological properties to the underlying macromolecular dynamics. Here, we perform macrorheology on composites of highly overlapping DNA and dextran polymers, focusing on the role of DNA topology (rings versus linear chains) as well as the relative volume fractions of DNA and dextran. On the same samples under the same conditions, we perform DDM and single-molecule tracking on embedded fluorescent-labeled DNA molecules immediately before and after bulk measurements. We show DNA-dextran composites exhibit unexpected nonmonotonic dependences of bulk viscoelasticity and molecular-level transport properties on the fraction of DNA comprising the composites, with characteristics that are strongly dependent on the DNA topology. We rationalize our results as arising from stretching and bundling of linear DNA versus compaction, swelling, and threading of rings driven by dextran-mediated depletion interactions. © *2022 The Society of Rheology.* https://doi.org/10.1122/8.0000447

I. INTRODUCTION

Ring polymers have been the topic of fervent investigation for decades due to their intriguing rheological and dynamical properties, biological significance, and industrial applications. For example, DNA naturally occurs in ring formation, and conversion between supercoiled and open circular (ring) topology plays a critical role in DNA replication and repair [1–3]. Further, ring polymers can tune the rheological properties of polymeric blends for commercial and industrial use [4–6]. While the dynamics of entangled linear polymers are well described by the reptation model developed by de Gennes [7] and Doi and Edwards [8], their extension to ring polymers is not straightforward due to their lack of free ends [9–11]. The extent to which ring polymers form entanglements and corresponding entanglement plateaus, the effect and persistence of threading of one polymer by another, and the relaxation modes available to ring polymers remain topics of debate [12–17].

Previous rheological studies have shown that entangled ring polymers do not display the same entanglement plateaus that their linear counterparts do [12,13,18–20], indicating a different rheological signature of the topological constraints in rings, generally referred to as entanglements. Entangled rings are predicted to adopt double-folded or amoebalike branched structures that undergo modified reptation that is faster than their linear counterparts [9,21–24]. At the same time, studies have shown that rings undergo very slow relaxation compared to entangled linear chains such that the final scaling of the storage and loss moduli in the terminal flow regime, $G'(\omega) \sim \omega^2$ and $G''(\omega) \sim \omega^1$, is not reached [12,17,25–28].

Simulations of concentrated ring polymer solutions have shown evidence of ring-ring threadings [29] that, for sufficiently overlapping large rings, manifest as glassy dynamics with kinetically arrested states and heterogeneous transport [30,31]. Within this framework, the rings adopt crumpled lattice-animal conformations with sufficient swelling and self-avoidance to allow for ring-ring threadings. Conversely, rings in dense solutions and melts have also been predicted to adopt collapsed double-folded structures, which are much less likely to become threaded [21,32,33]. Finally, simulations have shown that most rings are threaded by multiple rings with a wide range of threading lifetimes, for entanglement densities as low as $Z \approx 10$ entanglements per chain, prolonging their relaxation timescales and enhancing the dynamic heterogeneity [21,34,35].

In addition to ring-ring threading events, threading of rings by a small percentage of linear polymer "contaminants" that nearly all synthesis techniques produce likely also contribute to the reported slow relaxation of nominally "pure" entangled rings [36]. Linear DNA contaminants are also hard to avoid during purification and preparation of concentrated solutions of large ring DNA molecules, which have been studied extensively to elucidate the role of polymer topology on the dynamics of entangled polymer solutions [15,37–42]. Moreover, simulations have shown that the relaxation timescale of a threaded ring is significantly increased when threaded by multiple chains (rings or linear) versus a single

Note: This paper is part of the special issue on Ring Polymers.

[a)]Author to whom correspondence should be addressed; electronic mail: randerson@sandiego.edu

chain and that threading by linear chains is typically longer-lived than ring threading events [21,34]. The dominant relaxation mode of a ring with long-lived or multiple threadings is constraint release, whereby a polymer relaxes stress by the threading polymer unthreading itself and releasing its constraint [14,26,36], rather than the faster mode of reptation that otherwise dominates entangled polymer systems [8,23]. These diverse relaxation timescales associated with different topologies, sizes, and numbers of threading polymers give rise to heterogeneous dynamics in entangled "pure" rings and ring-linear blends [35,43,44], similar to those reported in simulations of entangled ring polymer solutions [30,31,45]. While the inclusion of linear chain threading is often needed to recapitulate stress relaxation in nominally "pure" ring melts, long-lived ring-ring threadings, along with multiple ring threading events, slow the dynamics considerably and are also predicted to contribute significantly to the slow relaxation of entangled rings [21,30,34].

The different rheological properties of entangled rings and linear polymers also manifest in the frequency dependence of the shear viscosity $\eta(\omega) \sim \omega^{-\gamma}$, an indicator of entanglements and how well polymers are able to align with shear flow. Highly entangled flexible linear polymer melts exhibit thinning $\eta(\omega) \sim \omega^{-\gamma}$ with $\gamma \approx 0.9 - 1$ [8,20], whereas entangled linear DNA solutions in good solvent conditions exhibit slightly reduced thinning with $\gamma \approx 0.6–0.9$ [16,46,47]. Entangled ring melts and solutions have been reported to exhibit weaker thinning than their linear counterparts ($\gamma \approx 0.4–0.6$) owing to their reduced ability to conformationally align with shear flow [16,20].

In ring-linear blends, threading of rings by linear chains has been shown to have profound effects on the rheology and dynamics [12,25,26,36,48–50], including emergent entanglement plateaus, increased zero-shear viscosity and thinning, suppressed relaxation, and hindered diffusion as compared to monodisperse systems of linear chains or rings [16,50–54]. For example, previous studies have shown that a small fraction of linear chains (>0.05) can cause entangled ring melts to transition from power-law stress relaxation [25,55] to exhibiting entanglement plateaus comparable to their linear counterparts [19]. At the same time, a small fraction of rings (up to ~0.3) added to entangled linear polymer melts has been shown to increase the viscosity up to ~2-fold [14,26]. Further, recent simulations have shown that rings in a melt of short linear polymers (up to ~10-fold shorter than the rings) exhibit more swollen conformations, due to excess chain-end free volume effects of the interpenetrating linear chains [54]. These swollen rings diffuse faster than in their own melt, demonstrating that any threading by the short linear chains is transient and actually enhances rather than restricts ring mobility. However, when the length of the surrounding linear chains exceeds the entanglement length, ring diffusion drops substantially owing to long-lived threadings by the entangled linear chains. Finally, the addition of linear chains to entangled rings increases the thinning exponent to be comparable to or larger than that for entangled linear polymers with reported values of $\gamma \approx 0.7–0.9$ [16,19], suggesting that threading of rings by linear chains aids in stretching and aligning rings along the flow direction.

While the role of polymer topology in entangled melts, solutions, and blends continues to be widely investigated, how topology modulates the rheology and dynamics of composites of two distinct polymeric species with different sizes, stiffnesses, and structures remains scarcely explored [56]. Free energy minimization of composites, typically comprising a polymer matrix and a "filler" species, leads to emergent behavior, such as nonmonotonic dependence of viscoelastic and transport properties on the relative fraction of each species [57–61]. Emergent phenomena in composites can arise from entropically driven polymer bundling and flocculation [56,60,62], enhanced miscibility and solubility [56,61,63,64], or even liquid–liquid phase separation [65,66].

For example, we previously showed that composites of flexible DNA and ~200-fold stiffer actin filaments exhibit enhanced stiffening and suppressed relaxation compared to networks of DNA or actin alone due to small-scale actin bundling, driven by DNA, that stiffens and strengthens the composite [60]. This phenomenon arises from depletion interactions, ubiquitous in biology, in which macromolecules of one species (actin) are driven together to maximize the available volume (and thus entropy) of the other smaller, faster, and/or more abundant species (DNA). The unexpected nonmonotonic dependence of composite stiffening on the actin fraction is a result of competition between actin bundling, which stiffens the actin network and suppresses thermal fluctuations, and actin network connectivity, which is required to provide a percolated scaffold to support and entangle with the DNA. Similar nonmonotonic emergence has been reported in crosslinked composites of cytoskeleton filaments [57,61,67]. The general phenomenon of depletion interactions driving opposing effects of increased polymer self-association and reduced polymer network connectivity, resulting in nonmonotonic dependences of dynamics on the varying fractions of the polymers and depletants, appears to be a signature of a wide range of polymer composites [56,60,68].

Similar emergent phenomena have also been shown to arise in composites of polymer and colloids [69–71] or nanoparticles (NPs) [72], which have been investigated extensively to understand the role of depletion interactions in composites [73]. For example, a recent study investigating the role of short chains added to composites of long polymers and NPs reported a nonmonotonic dependence of composite strength on the ratio of short, NP-adsorbing polymers and long linear polymers [72]. The peak in mechanical strength, which occurs at ~40% short chains, is attributed to an optimal balance of long-chain stretching and thus increased overlap density with reduced polymer entanglements and connectivity as the number of long NP-bridging polymers is reduced. The competition between enhanced polymer self-association and network connectivity is similar in spirit to that reported in other composite systems [56,60,68].

Similar to [72], we previously found stretching of tracer linear DNA from random coils to elongated snake-like conformations when crowded by small dextran polymers at sufficient dextran volume fraction (~30%, $11c^*$) [74]. Conversely, ring DNA condensed into more compact spherical conformations under the same conditions [75]. Both elongation and compaction are volume-minimizing conformations, driven by entropy

maximization of the dextran crowders (i.e., the depletion interaction). These studies also examined the diffusion of the tracer DNA crowded by dextran, reporting subdiffusive dynamics for linear DNA at short lag times ($\Delta t < 10$ s) and normal diffusion for longer lag times ($10\,\text{s} < \Delta t < 50\,\text{s}$) [74]. Conversely, ring DNA exhibited normal diffusion across all lag times [75]. For $\Delta t > 10$ s, the diffusion coefficients for both ring and linear DNA decreased with increasing dextran concentration, but with more modest scaling than classically expected owing to their volume-minimizing conformations.

The complex and intriguing effects of polymer end-closure on rheology and macromolecular dynamics [10,18,20,76], combined with the rich emergent phenomena that polymer composites exhibit [58,68,77–79], motivated us to examine the molecular-level transport and bulk rheological properties of concentrated composite solutions of DNA and dextran (Fig. 1). We fix the polymer overlap in all cases and investigate solutions of linear DNA and dextran with varying volume fractions of DNA ϕ. We compare our results for each ϕ with those of a more complex composite system in which

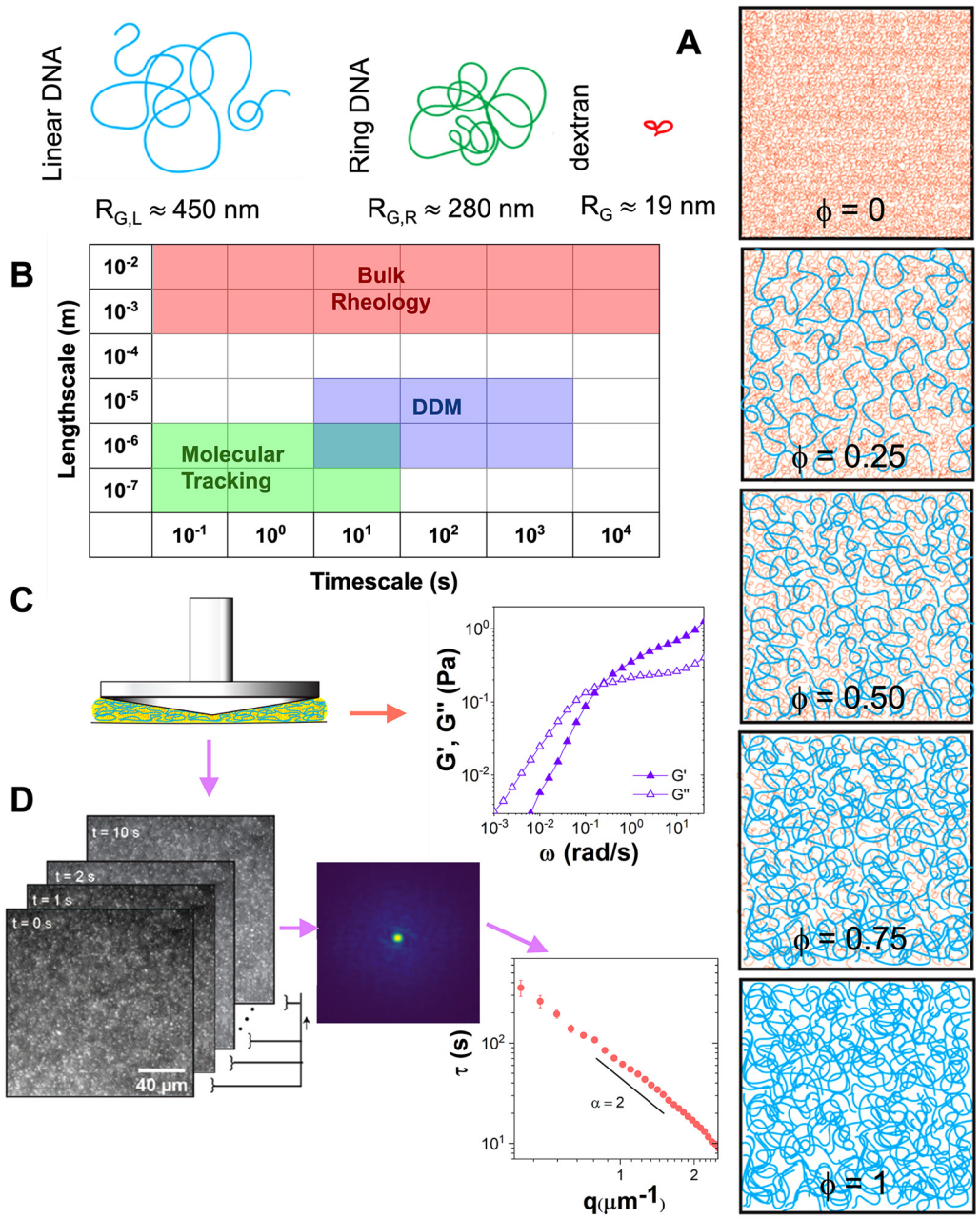

FIG. 1. Experimental platform to investigate bulk rheology and molecular-level dynamics in composites of DNA and dextran. (a) Cartoon of macromolecules that comprise the composites, with their corresponding radius of gyration R_G listed: 25-kbp linear DNA, 25-kbp ring DNA, and 500 kDa dextran. The panel on the right depicts $11c^*$ composites of linear DNA and dextran at all DNA volume fractions ϕ that we investigate: $\phi = 0$ (100% dextran), $\phi = 0.25$ (25% DNA, 75% dextran), $\phi = 0.50$ (50% DNA, 50% dextran), $\phi = 0.75$ (75% DNA, 25% dextran), and $\phi = 1$ (100% DNA). (b) Lengthscales and timescales probed by the different techniques we use: bulk rheology, DDM, and molecular tracking. (c) We use a DHR3 rheometer to measure bulk viscoelastic properties of composites, including the elastic and viscous moduli $G'(\omega)$ (filled symbols) and $G''(\omega)$ (open symbols). (d) Immediately before and after bulk rheology measurements, we capture time-series of labeled DNA molecules diffusing in the sample using the fluorescence microscopy capabilities of the rheometer. We perform DDM analysis on captured time-series to determine the image structure function $D(q, \Delta t)$ as a function of lag time, Δt, and wave vector, q. By fitting $D(q, \Delta t)$, we determine the density fluctuation decay times τ as a function of q to describe the DNA dynamics. Data shown in (c) and (d) are for linear DNA at $\phi = 1$.

we replace 90% of the linear DNA with ring DNA (keeping 10% linear) while maintaining ϕ.

Our work elucidates the dynamics of these complex DNA-dextran composite solutions from the scale of single polymers ($\sim 10^2$ nm) to that of the macroscopic bulk (~cm). Specifically, we couple macrorheology with fluorescence microscopy, differential dynamic microscopy (DDM), and single-molecule tracking (SMT) to directly connect the bulk rheological properties of the composite solutions to the microscale transport properties of the comprising DNA.

While both macro- and micro-rheological techniques have been extensively used to investigate entangled polymers and other soft materials, these distinct measurements are typically performed on different samples with different preparation methods, chamber geometries, and sample volumes [80,81]. As such, a direct connection between the properties at these two scales is nontrivial [47,82–84]. We overcome these limitations by performing imaging and rheology measurements in the same sample using a rheometer with high-speed fluorescence imaging capabilities. Further, we track DNA molecules comprising the composites, rather than embedded probes (as is typically done in microrheology experiments [85]), to directly report macromolecular dynamics via DDM.

Our results reveal a surprising nonmonotonic dependence of the rheological properties on the fraction of DNA comprising the composites, with 75%–25% DNA-dextran composites exhibiting uniquely suppressed dissipation coupled with prolonged relaxation times and subdiffusion. We argue that this emergent behavior, that is strongly dependent on DNA topology, arises from entropically driven self-association and stretching of linear DNA versus swelling and threading of ring DNA.

II. MATERIALS AND METHODS

A. DNA

We prepare solutions of double-stranded DNA, 25 kbp in length, via replication of fosmid constructs in *Escherichia coli* followed by extraction, purification, and concentration as described previously [86–88]. Briefly, to replicate DNA, *E. coli* cultures containing the fosmid clone are grown from frozen glycerol stocks. To extract the DNA, cells are lysed via treatment with an alkaline solution. The extracted DNA is then renatured via treatment with an acidic detergent, precipitated in isopropanol, washed with 70% ethanol, and resuspended in TE10 buffer [10 mM Tris-HCl (pH 8), 1 mM EDTA, 10 mM NaCl]. To purify the DNA, the solution is treated with RNase A (to remove contaminating RNA) followed by phenol-chloroform extraction and dialysis (to remove proteins). We assess purity using UV absorbance and gel electrophoresis [87]. The purified DNA solution has a 260/280 absorbance ratio of ~1.8, in the accepted range for pure DNA with minimal protein contaminants [89], and no detectable RNA (which manifests as a low MW smear on a gel) (Fig. S1) [120].

We use gel electrophoresis to determine a concentration of 3.25 mg/ml our purified solution, consisting of ~90% relaxed circular (ring) and ~10% linear DNA (Fig. S1) [120]. Gel analysis is performed using Life Technologies E-GEL IMAGER and GEL QUANT EXPRESS software (Fig. S1) [120]. We convert half of the purified stock DNA solution to linear topology via treatment with the restriction enzyme ApaI (New England Biolabs). We confirm complete conversion to linear topology via gel electrophoresis (Fig. S1) [120].

The radii of gyration for the ring and linear DNA are $R_{G,R} \simeq 280$ nm and $R_{G,L} \simeq 450$ nm, respectively [88]. We compute polymer overlap concentrations for the linear and 90% ring DNA solutions via $c^* = (3/4\pi)(M/N_A)/(f_L R_{G,L}^3 + (1 - f_L) R_{G,R}^3)$, where M is the molecular weight and f_L is the fraction of linear DNA in the sample ($f_L = 1$ and 0.1 for linear and ring solutions, respectively) [8,90], resulting in $c_{90R}^* \simeq 220$ μg/ml and $c_L^* \simeq 71$ μg/ml for ring and linear DNA, respectively. We note that our c^* calculations assume random coil configurations of similar size to the dilute condition and do not account for any swelling or compaction that may arise in the entangled and crowded systems studied here. To image DNA for DDM and SMT, we fluorescent-label a fraction of the DNA molecules with MFP488 (Mirus) using the manufacturer-supplied *Label* IT Labeling Kit and corresponding protocols (Mirus). The excitation/emission spectrum for MFP488 is 501/523 nm, and the dye molecule to DNA base pair ratio is 5:1.

B. Dextran

We use molecular biology grade dextran (Fisher BioReagents BP1580100, Lot #196289), with a molecular weight of 500 kDa and $R_G \simeq 19$ nm [91]. The manufacturer-provided certificate of analysis shows suitability for protein fractionation and gel permeation chromatography, with heavy metal impurities and ignition residues below industry standards for molecular biology grade purity. To prepare composites, dextran is dissolved in TE10 buffer at a concentration of 28.9 mg/ml ($11c^*$) and homogenized via slow rotation at room temperature for >24 h. In the present study, as well as our previous studies investigating the diffusion of tracer DNA in crowded dextran solutions [74], we see no signs of adsorption or other nonsteric interactions between dextran and DNA.

C. Sample preparation

We prepare each sample at a volume of 350 μl comprising different volume fractions of DNA and dextran solutions each at $11c^*$, corresponding to 2.42, 0.78, and 28.9 mg/ml for ring DNA, linear DNA, and dextran, respectively. We add 2 μl of labeled ring or linear DNA tracers to each sample for microscopy measurements. Each sample is prepared at least 4 days prior to experiments and rotated at 4 °C to mix and equilibrate. An oxygen scavenging system (45 μg/ml glucose, 43 μg/ml glucose oxidase, 7 μg/ml catalase, 0.005% β-mercaptoethanol) is added to inhibit photobleaching. Composites comprising both DNA and dextran are prepared by mixing varying volume fractions of $11c^*$ DNA and dextran solutions, which we quantify by the volume fraction of the DNA solution ϕ. We investigate samples with $\phi = 0$ (0% DNA, 100% dextran) $\phi = 0.25$ (25% DNA, 75% dextran), $\phi = 0.5$ (50% DNA, 50% dextran), $\phi = 0.75$ (75%

DNA, 25% dextran), and $\phi = 1$ (100% DNA, 0% dextran). For each ϕ, we prepare samples using either the linear DNA solution or the 90-10 ring-linear DNA solution (which we refer to as "90-ring" throughout the paper).

D. Rheometry

We use a Discovery Hybrid Rheometer 3 (DHR3, TA Instruments) with a 1° steel cone geometry to perform bulk rheology measurements. We use a glass slide as the bottom plate to enable imaging of fluorescent-labeled DNA in the samples. To prevent evaporation during the experimental cycle, we apply mineral oil around the geometry and the sample. To measure linear viscoelastic moduli, $G'(\omega)$ and $G''(\omega)$, we perform two identical frequency sweeps from $\omega = 0.001$ to 100 rad/s at 5% strain (well within the linear regime as determined by amplitude sweeps). Each frequency sweep lasts ~6.5 h with individual frequency measurements spaced 30 min apart. All data shown are above the measurable torque minimum of 0.5 nN m for the DHR3 rheometer.

E. Fluorescence microscopy

The DHR3 is outfitted with a Modular Microscope Accessory (TA Instruments) with a 40× 0.6 NA objective (Nikon), blue-light LED source, 490/525 nm excitation/emission filters, and a Hamamatsu ORCA-Flash 2.8 CMOS camera to enable imaging of MPF488-labeled DNA in the blends. Immediately before and after each bulk rheology measurement, we collect three 512×512 pixel videos of 2000 frames at 1 fps. We use 2×2 pixel binning to improve signal to noise, resulting in 256×256 images with an effective pixel size of 0.312 μm. This binning, along with the dense concentration of labeled DNA in each field-of-view (Fig. S2) [120], is optimized for statistically robust DDM measurements. However, it prohibits accurate measurement of changes to the conformational size and shape of individual DNA molecules. Sample frames from before and after videos are shown in Fig. S2 [120].

F. Differential dynamic microscopy

For DDM analysis, we split the videos into 256×256 pixel regions of interest (ROIs) which we analyze separately. We use custom-written scripts (PYTHON) to perform DDM. For standard DDM analysis, one takes two-dimensional Fourier transforms of differences between images separated by a range of lag times Δt in order to quantify how the degree of correlation decays with lag time as a function of the wave vector q. Because this standard correlation function is sensitive to global drift of the sample, we use a slightly modified correlation function referred to as the far-field DDM (FF-DDM) function. Previous work has shown that by using FF-DDM, the DDM correlation function, $D(q, \Delta t)$, is less sensitive to drift [92,93]. As with standard DDM analysis, we fit the FF-DDM matrix to $D(q, \Delta t) = A(q)[1 - f(q, \Delta t)] + B(q)$, where $f(q, \Delta t)$ is the intermediate scattering function (ISF), $A(q)$ is the amplitude, and $B(q)$ is the background. To determine the type of motion and the corresponding rate, we model the ISF as a stretched exponential: $f(q, \Delta t) = e^{-(\Delta t/\tau(q))^{\gamma}}$, where $\tau(q)$ is the decay time and γ is the stretching exponent. The use of a stretched exponential as opposed to a simple exponential has been shown to better fit dynamics in confined or entangled systems [94,95]. Scaling of $\tau(q) \sim q^{-2}$ is indicative of normal Brownian diffusion [i.e., mean-squared displacement $(MSD) \sim t$], whereas a decay time that depends less strongly on q has been associated with more arrested or confined motion [96,97]. Error bars are standard error across all ROIs and videos, representing sample-to-sample variation. Example ISFs and fits are shown in Fig. S4 [120] and sample-to-sample variation in the ISFs is shown in Fig. S5 [120]. Estimates of diffusion coefficients D and their errors are based on fits to $\tau(q) = 1/Dq^2$ over the range of q from 0.39 to 2.44 μm^{-1}. For some samples, particularly for $\phi = 0.75$ composites, we observe a q-dependence that indicates nearly arrested rather than diffusive dynamics [97]. While we still compute an effective diffusion coefficient for these samples, because the dynamics differ from normal diffusive transport, we also fit each curve to $\tau(q) = 1/Kq^{\alpha}$ where α is a free parameter that is ~2 for normal diffusion and approaches zero for halted or arrested dynamics. K is the generalized transport coefficient that is equivalent to D when $\alpha = 2$.

G. Single-molecule tracking

For SMT experiments, we image the MFP488-labeled DNA using an Olympus IX73 inverted fluorescence microscope with a 60×1.2 NA oil immersion objective (Olympus). We collect five 512×512 pixel videos of 2000 frames at 10 fps for each sample. We use custom particle-tracking scripts (Python) to track the center-of-mass of individual DNA molecules and measure their frame-to-frame x and y displacements $(\Delta x, \Delta y)$ from which we compute the ensemble averaged MSDs $\left(\langle \Delta x^2 \rangle, \langle \Delta y^2 \rangle\right)$. We fit the average of $\langle \Delta x^2 \rangle$ and $\langle \Delta y^2 \rangle$ (i.e., MSD) versus lag time Δt to a power-law function $MSD \sim \Delta t^{\beta}$, where β is the subdiffusive scaling exponent. For a system exhibiting normal diffusion, $\beta = 1$, while $\beta < 1$ indicates anomalous subdiffusion. Error bars are based on fits of the data to $MSD \sim \Delta t^{\beta}$.

III. RESULTS AND DISCUSSION

A. System details

In all of our experiments, we fix the total polymer concentration to $11c^*$ to ensure that the molecules are highly overlapping, and we vary the volume fractions of the $11c^*$ solutions of the different polymers (ring DNA, linear DNA, and dextran). By fixing the degree to which molecules overlap, we can unambiguously determine the effect of polymer topology (i.e., ring versus linear DNA), as well as steric and entropic interactions between distinct polymers (i.e., DNA and dextran), on the rheological properties and macromolecular dynamics. Specifically, we examine DNA-dextran blends with either purely linear DNA or 90-10 ring-linear DNA (which we abbreviate as "90-ring"

throughout the paper) at DNA volume fractions of $\phi = 0$ (pure dextran solution), 0.25, 0.5, 0.75, and 1 (pure DNA solution).

B. Bulk linear rheology of DNA-dextran composites

We first examine the bulk linear viscoelastic properties of DNA-dextran composites. Figure 2(a) compares the elastic modulus $G'(\omega)$ and viscous modulus $G''(\omega)$ for composites with linear DNA (left plot) and ring DNA (right plot). Pure dextran solutions (not shown) exhibit Newtonian properties with $G'' \sim \omega^1$ scaling over the entire frequency range. Linear DNA solutions without dextran ($\phi = 1$) show a transition from the terminal flow regime at low frequencies, with approximate scaling of $G'' \sim \omega^1$ and $G' \sim \omega^2$, to a rubbery plateau at high frequencies with a crossover frequency, at which G' exceeds G'', of $\omega_D \approx 0.25$ rad/s. This crossover frequency is a measure of the disengagement time, $\tau_D \approx 2\pi/\omega_D \approx 25$ s, which is the relaxation time associated with an entangled polymer reptating out of its confining tube. Different from linear DNA, 90-ring DNA solutions ($\phi = 1$) exhibit an elastic rubbery plateau over the entire frequency range, indicating very slow relaxation mechanisms at play ($\tau > 100$ min), as previously reported and predicted for nominally pure ring melts and ring-linear blends with low fractions of linear chains [12,17,25–28,30].

This slow relaxation has also been predicted to arise in concentrated solutions of pure rings and those with linear "contaminants" (as in our 90-ring solution) due to threading of rings by neighboring rings and linear chains, with the

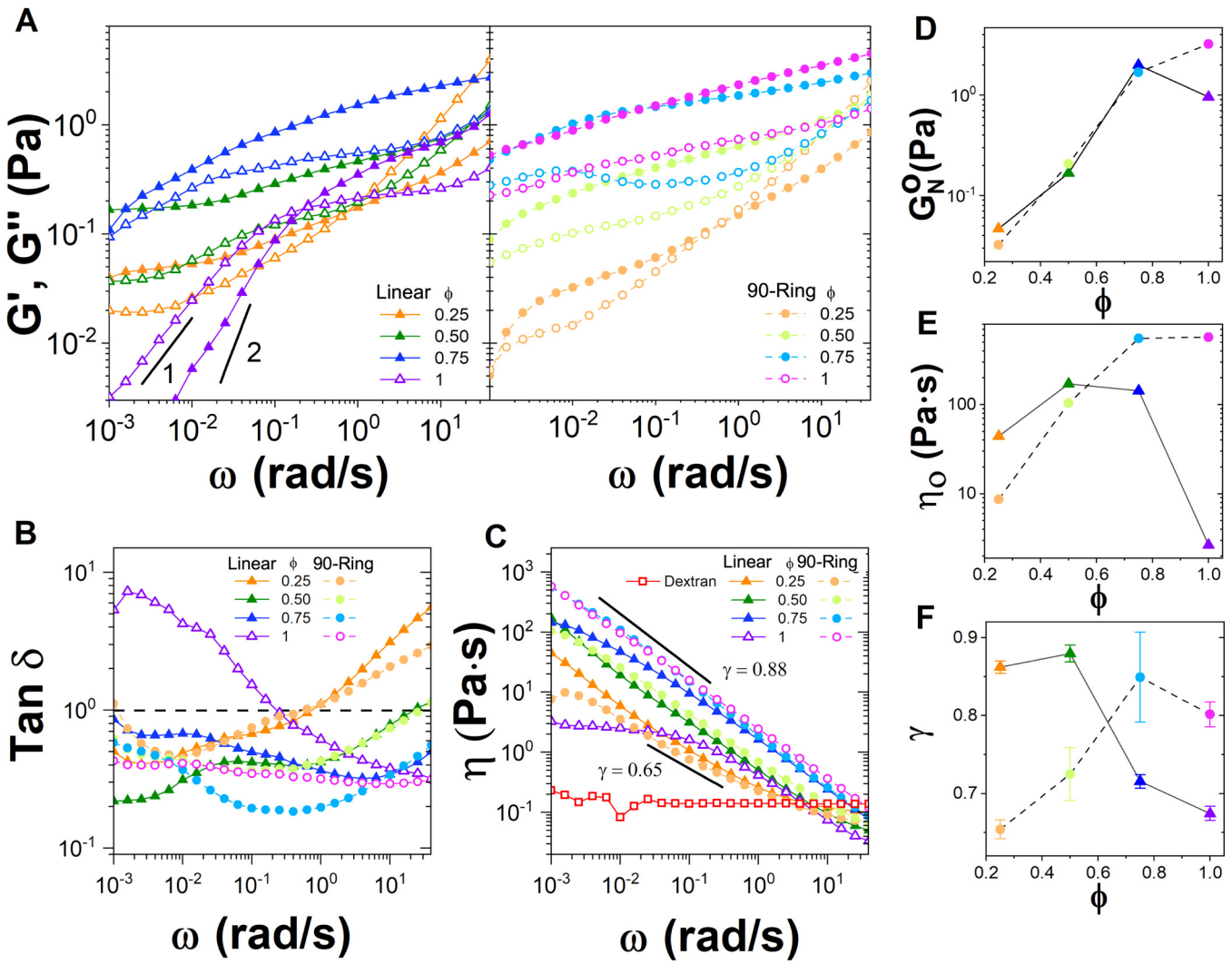

FIG. 2. Bulk linear rheology of DNA-dextran composites exhibits complex dependence on the topology and volume fraction of DNA. (a) Elastic modulus G' (closed symbols) and viscous modulus G'' (open symbols) as a function of frequency ω for DNA-dextran composites with linear DNA (left panel, triangles, dark shades) and 90-ring DNA (right panel, circles, light shades) at volume fractions of $\phi = 0.25$, 0.5, 0.75, and 1, as indicated in the legend. Terminal regime scalings $G'(\omega) \sim \omega^{-2}$ and $G''(\omega) \sim \omega^{-1}$ are indicated by the scale bars in the left panel. (b) Loss tangent $\tan\delta = G''(\omega)/G'(\omega)$ for data shown in (a). For clarity, pure DNA solutions ($\phi = 1$) are denoted by open symbols. Dashed line denotes $\tan\delta = 1$ which corresponds to low and high crossover frequencies, $\omega_D = 2\pi/\tau_D$ and $\omega_e = 2\pi/\tau_e$, respectively. (c) Complex viscosity $\eta(\omega) = [G''(\omega)^2 + G'(\omega)^2]^{1/2}/\omega$ of composites shown in (b) and a pure dextran solution ($\phi = 0$, open squares). All composites exhibit complex viscosity thinning $\eta(\omega) \sim \omega^{-\gamma}$ with exponents γ that vary from ~0.65 to ~0.88. (d) Plateau modulus G_N^0 versus ϕ for composites with 90-ring (circles, dashed connecting line) and linear (triangles, solid connecting line) DNA. G_N^0 is computed by evaluating G' at the frequency in which $\tan\delta$ is a minimum. (e) Zero-shear viscosity $\eta_0 = \eta(\omega \to 0)$ versus ϕ for composites with ring (circles, dashed connecting line) and linear (triangles, solid connecting line) DNA determined from $\eta(\omega)$ curves shown in (c). (f) Complex viscosity thinning exponent γ versus ϕ determined from power-law fits to the data shown in (c). Error bars are determined from fits to the data.

number of threading polymers increasing the threading lifetime [30,31,45]. Given the relatively small size of our rings ($N = 83$ where N is the number of Kuhn lengths l_k) we do not expect a large number of threadings per ring [43]. As such, because the threading lifetime for linear chains is predicted to be slower than that for rings, we expect that threading by the 10% linear chains plays an important role in the suppressed relaxation and extended rubbery plateau we observe.

In contrast to previous studies on ring and linear polymer melts [19,25], the magnitude of the plateau modulus G_N^0 for 90-ring DNA is several times larger than that for linear DNA. To shed light on this discrepancy, we quantify G_N^0 for all solutions by evaluating G' at the frequency at which the corresponding loss tangent $\tan\delta = G''(\omega)/G'(\omega)$ [Fig. 2(b)] is a minimum [98]. For cases in which a frequency-independent plateau is not apparent, G_N^0 should be considered approximate. We find $G_N^0 \simeq 3.24$ and $\sim$0.96 Pa for 90-ring and linear DNA solutions, respectively, such that $G_{N,R}^0/G_{N,L}^0 \simeq 3.4$ [Fig. 2(d)]. From G_N^0, we can estimate the polymer length between entanglements l_e via $l_e = 4cRT/5G_N^0 M_{BP}$, where c is the mass concentration and $M_{BP} \approx 650$ g/mol is the molecular weight of a DNA base pair ($\sim$1/3 nm) [8,23]. For linear DNA, we find $l_e \simeq 833$ nm and the number of entanglements per chain $N_e \approx 10$. As described in Sec. II, to maintain concentration at $11c^*$, the mass concentration of the nominal ring sample is $\sim$3-fold higher than for the linear sample ($11c_{90-R}^*/11c_L^* \simeq 2.42/0.78 \simeq 3.1$) due to the smaller R_G of rings. As $l_e \sim c/G_N^0$, the $\sim$3-fold larger G_N^0 and c for rings is consistent with the fact that we are fixing the degree of polymer overlap and thus l_e. As such, while a $\sim$3.4-fold higher G_N^0 value is, at first glance, at odds with previous studies [19,25,36], the increased mass concentration of our 90-ring solutions compared to our linear DNA solutions accounts for this increase.

Upon mixing DNA with dextran (thereby decreasing ϕ), we find that the dependence of G_N^0 on DNA topology is substantially reduced, with values for 90-ring and linear composites differing by $\leq 1.5x$. Future studies will focus on the $\phi > 0.75$ regime to determine the onset of more pronounced topology dependence of G_N^0, as seen in pure DNA solutions ($\phi = 1$). Comparing the effect of varying ϕ on the 90-ring and linear DNA, we find that G_N^0 for 90-ring DNA decreases when mixed with dextran, while for linear DNA, G_N^0 displays a nonmonotonic dependence on ϕ with a maximum at $\phi = 0.75$.

For both topologies, $\phi \leq 0.5$ blends display a high frequency crossover ω_e in which $G'' > G'$, which is a measure of the entanglement time $\tau_e \approx 2\pi/\omega_e$ or the time it takes for an entangled polymer to "feel" its tube confinement [8]. This crossover frequency increases from $\sim$0.63 at $\phi = 0.25$ to $\sim$25 rad/s at $\phi = 0.5$, independent of DNA topology, and is nonexistent for $\phi = 0.75$ and 1 (implying $\omega_e > 100$ rad/s). These values correspond to $\tau_e \approx 10$, 0.25, and <0.06 s, for $\phi = 0.25$, 0.5, and >0.5. The independence of τ_e on topology can be understood as arising from the matching of l_e. Namely, $\tau_e \sim a^4/D_0 R_{G,0}^2$, where $a \approx (l_K l_e)^{1/2}$ is the entanglement tube diameter, l_K is the Kuhn length ($\sim$100 nm for dsDNA), and D_0 and $R_{G,0}$ are the diffusion coefficient and radius of gyration in the dilute limit [8,23,99]. Insofar as $D_{0,R}/D_{0,L} \approx 1.32$, $R_{G,0,L}/R_{G,0,R} \approx 1.58$ [87], and $l_{e,L} \approx l_{e,R}$, we find $\tau_{e,R} \approx 1.8\tau_{e,L}$ such that, within the factor of two frequency resolution of our measurements, we can estimate $\tau_{e,R} \approx \tau_{e,L}$.

Further, if we only consider the DNA in the composites and use the relations $\tau_e \sim l_e^2$, $l_e \sim c/G_N^0$ and $G_N^0 \sim c^2$ [8], it follows that l_e decreases as ϕ increases (i.e., $l_e \sim c^{-1} \sim \phi^{-1}$) so τ_e is likewise expected to decrease, as we find in composites. The decrease in τ_e between $\phi = 0.25$ and 0.50 is stronger than the predicted scaling (i.e., $\tau_e \sim l_e^2 \sim \phi^{-2}$), with an approximate scaling of $\tau_e \sim \phi^{-5.3}$. This increased ϕ dependence may indicate that dextran increases the entanglement density and overlap of DNA via depletion interactions, which causes l_e to decrease more strongly than expected with increasing ϕ. An alternative explanation is that the $\phi = 0.25$ and $\phi = 0.50$ composites span different scaling regimes [100]. While $G_N^0 \sim \phi^2$ generally holds for entangled flexible linear polymers, semidilute solutions of flexible and semiflexible linear chains are predicted to follow a steeper scaling $G_N^0 \sim \phi^{9/4}$, which leads to a stronger ϕ dependence of $\tau_e \sim l_e^2 \sim (\phi^{-5/4})^2 \sim \phi^{-5/2}$. At low ϕ values (0.25 and 0.5), ignoring the effect of dextran, the DNA is indeed in the semidilute limit so this steeper scaling may likely apply.

Moreover, in the semidilute model, G_N^0 also increases with increasing Kuhn length l_k such that $G_N^0 \sim \phi^{9/4} l_k^{19/4}$ and $G_N^0 \sim \phi^{9/4} l_k^{11/4}$ for flexible and semiflexible polymers, respectively. Depletion-driven bundling of DNA by dextran, facilitated by the previously reported dextran-mediated elongation of linear DNA from random coil configuration [74], may indeed serve to "stiffen" the (bundled) DNA (i.e., reduce its susceptibility to thermal bending), thereby increasing l_k and pushing the flexible DNA toward the semiflexible regime. Within this framework, we expect $\tau_e \sim l_e^2 \sim (\phi/G_N^0)^2 \sim (\phi^{-5/4} l_k^{-11/4})^2$, with l_k increasing with increasing ϕ as DNA overlap and bundling increases (and the entanglement spacing decreases). For semiflexible polymers, the mesh size, which scales as $\xi \sim \phi^{-1/2}$ [101], provides a measure of this entanglement spacing [102]. As such, keeping all other scaling assumptions, and phenomenologically estimating $l_k \sim \xi^{-1} \sim \phi^{1/2}$, provides $\tau_e \sim \phi^{-5/2} l_k^{-11/2} \sim \phi^{-5/2}\phi^{-11/4} \sim \phi^{-5.3}$, matching our empirical scaling. We note that this scaling argument should not be considered quantitative as it draws on theoretical assumptions that span different regimes, and the empirical scaling is determined from two data points. Nevertheless, the scaling arguments indicate that dextran-mediated interactions likely play a principal role in the steep scaling we see at low ϕ by increasing the DNA entanglement density and stiffness (i.e., reducing l_e and increasing l_k) by elongation and small-scale bundling.

To incorporate the effect of dextran, we use our estimated G_N^0 values [Fig. 2(d)], along with $l_e \sim \phi/G_N^0$ and $l_{e,DNA} \approx 833$ nm, to estimate l_e for the different composites. This analysis (Fig. S3) [120] shows that, for linear DNA, the $\phi = 0.75$ composites have the smallest predicted l_e ($\sim$300 nm), whereas for rings, $\phi = 1$ solutions have the lowest ($\sim$833 nm). Taken together, these results suggest that the peak in G_N^0 at $\phi = 0.75$ for linear DNA may be due to dextran-mediated DNA self-association and increased DNA

overlap. However, this effect appears to play a lesser role for 90-ring DNA, as it reaches the highest apparent degree of overlap (i.e., minimum l_e) without dextran ($\phi = 1$).

Further examination of the loss tangent [Fig. 2(b)] shows that, for linear DNA composites, the rubbery plateau, flanked by the low and high frequencies at which $\tan\delta = 1$ (i.e., ω_D and ω_e) shifts to longer timescales (lower ω) and extends over a wider ω range when mixed with dextran. We also see that $\tan\delta$ generally increases with ω for $\phi \leq 0.5$ composites whereas the opposite is true for $\phi > 0.5$. This qualitatively different ω dependence is reminiscent of the difference between rheological properties of extended semiflexible polymers, such as actin filaments, which exhibit solid-like behavior at low ω and viscous-dominated flow at high ω [103], compared to entangled flexible random coil polymers (e.g., DNA) that display low-ω flow and high-ω rubber-like elasticity. This effect may indicate that dextran polymers are acting as depletants to extend and bundle linear DNA molecules, making them more akin to extended semiflexible polymers, as we suggest above [68,72,75]. As the DNA concentration increases and the dextran concentration decreases, the depletion-driven bundling becomes weaker while DNA-DNA entanglements are more abundant, so the frequency dependence is more akin to that of flexible polymers but the modulus is higher. Thus, the maximum in $G^0_{N,L}$ at $\phi = 0.75$ suggests an optimal combination of DNA overlap and depletion-driven stretching and bundling. Below $\phi = 0.75$, the DNA in the composite has fewer entanglements (Fig. S3) [120], so reinforcement from bundling comes at the cost of losing connectivity, thereby reducing $G^0_{N,L}$. We note that while we expect bundling to play a primary role in the rheology we measure, we expect bundles to be limited to only a few DNA chains such that high connectivity is preserved at $\phi = 0.75$. This expected small-scale bundling is below the resolution limit of our imaging setup (see Sec. II), similar to the actin bundling reported in actin-DNA composites [60].

For 90-ring composites, the rubbery plateau is truncated at short times (high ω) in $\phi = 0.25$ and 0.5 composites compared to $\phi = 0.75$ and $\phi = 1$ cases in which the plateau regime fully spans over four decades. Further, compared to linear DNA composites, there is limited ϕ dependence at low ω, suggesting that stiffening of rings via bundling and/or elongation plays minimal roles in 90-ring composites. We suggest instead that the variation in threading propensity of rings dominates the rheology for ring composites. Previously, we found that high dextran concentrations (>10c^*) led to compaction of ring DNA, rather than elongation [75], which would result in fewer entanglements and more viscous-dominated rheology compared to a ring DNA solution at the same degree of overlap, as shown in Fig. 2(a). Further, due to >10× smaller coil size of dextran compared to DNA rings, the ability for dextran to kinetically pin rings via long-lived threading events is likely minimal.

Indeed, rings in a melt of short (unentangled) polymer chains have been shown to diffuse faster than when in their own melts and adopt more swollen conformations due to the interpenetrating linear chains [54]. It is important to clarify that in this regime the short linear chains are, in fact, threading the rings, but the effect of threading is to swell the rings and reduce the local chain density due to chain-end effects, thereby increasing, rather than decreasing, ring mobility. Threading by linear chains only slows the DNA when the threading linear chains become long enough to be sufficiently entangled, which is not the case for our high ϕ (i.e., low dextran fraction) 90-ring composites.

Such swelling, which may occur for higher DNA volume fractions (versus compaction observed for higher dextran fractions), likely facilitates ring-ring and ring-linear DNA threading in composites that suppress relaxation. Swelling will also limit the fraction of double-folded and amoebalike ring conformations that can undergo modified reptation but are not threaded [21,104]. Thus, in the $\phi = 0.75$ ring composite, the relaxation is likely entirely due to the constraint release of threaded DNA, while the $\phi = 1$ DNA solution has both reptation and threading contributions. This effect can be seen in Fig. 2(b) in which $\tan\delta$ for the $\phi = 0.75$ ring composite is smaller than that for $\phi = 1$ over most of the frequency range ($\omega \approx$ 0.006–6 rad/s), indicating the timescale over which threading, which occurs more frequently at $\phi = 0.75$ than $\phi = 1$, dominates ($t_{th} \approx 1$ to $\sim 10^{-3}$ s). Above and below this timescale, unthreaded and unswollen rings in $\phi = 1$ solutions may still "feel" the constraints of the entanglement tube (no measurable τ_e) and be confined to reptate within it (no measurable τ_D).

Finally, we evaluate the complex viscosity $\eta(\omega)$ [Fig. 2(c)], and, assuming that the Cox–Merz rule is valid for our solutions [16,18,47,105–107], we estimate the zero-shear viscosity $\eta_0 = \eta(\omega \to 0)$ [Fig. 2(e)] and corresponding thinning exponent γ [Fig. 2(f)] by fitting each curve to a power-law $\eta(\omega) \sim \omega^{-\gamma}$. Because only the linear DNA solution and $\phi = 0.25$ 90-ring composite exhibit low-frequency plateaus, our η_0 values for the other cases should be taken as lower limits. As shown in Fig. 2(e), we find that η_0 for linear DNA composites exhibit a nonmonotonic dependence on ϕ, corroborating our interpretation of depletion-driven stretching and bundling of linear DNA in composites.

Conversely, for 90-rings, η_0 increases monotonically with ϕ, in agreement with previous studies showing that dilute rings in a melt of short linear chains (akin to low ϕ composites) have lower viscosity than for pure rings [54]. Further, η_0 is maximum at $\phi = 1$ rather than $\phi = 0.75$ because η_0 is evaluated in the long-time limit such that $t > t_{th}$, so threading events are no longer constraining the rings but tube confinement is still present, as indicated in Fig. 2(e). The latter is more prevalent for $\phi = 1$ 90-ring solutions compared to $\phi = 0.75$ composites.

We next examine the complex viscosity thinning exponents [Fig. 2(f)], which provide insight into the ability of entangled polymers to align with flow [18,108,109]. For highly entangled linear polymer melts, $\eta(\omega) \sim \omega^{-1}$, while thinning exponents of $\gamma \approx 0.6$–0.9 have been reported for solutions of entangled linear DNA [16,20]. Previous studies on entangled rings report reduced thinning exponents of $\gamma \approx$ 0.4–0.6 [16,20], owing to the reduced ability of rings to stretch along the shear direction. Our previous studies on ring-linear DNA blends showed a maximum in γ with comparable concentrations of rings and linear chains, in which threading by linear chains was most pervasive, suggesting that threading by linear chains facilitates flow alignment of

rings [16]. Moreover, if we assume rings are compacted by dextran at low ϕ while linear chains are stretched and bundled, we would expect minimal flow alignment and thinning for rings and maximal alignment for linear chains at $\phi = 0.25$ and 0.5, which is indeed what we see. For $\phi > 0.5$, γ drops significantly for linear DNA composites whereas it increases a comparable amount for 90-ring DNA composites. Thus, for rings, threading by linear chains, mediated by chain swelling, appears to promote thinning whereas for linear chains it is the depletion-driven elongation and increased overlap that drives thinning.

C. DDM to determine macromolecular transport properties

To shed light on the macromolecular dynamics that give rise to the bulk rheological properties discussed above, we use an optical microscopy attachment to our rheometer to collect time-series of images of diffusing linear and ring DNA in the composites (Fig. S2) [120] and perform DDM analysis on the time-series to determine their transport properties (Fig. 3) [110,111]. Importantly, these data are collected in the exact samples and geometry as bulk rheology data immediately before and after rheology measurements (see Sec. II).

Some key questions we seek to answer with this analysis are (1) if ring DNA solutions and composites exhibit glassy dynamics, (2) if mixing of linear DNA with dextran slows its diffusion and/or alters its transport properties, (3) the extent to which the relaxation and diffusive mechanisms that rings and linear chains exhibit in the different conditions are similar or different, and (4) if the topology and ϕ dependence of bulk rheological properties manifest at the molecular level or if there are scale-dependent phenomena that arise, as seen in other entangled polymer solutions and composites [47,84,112–114].

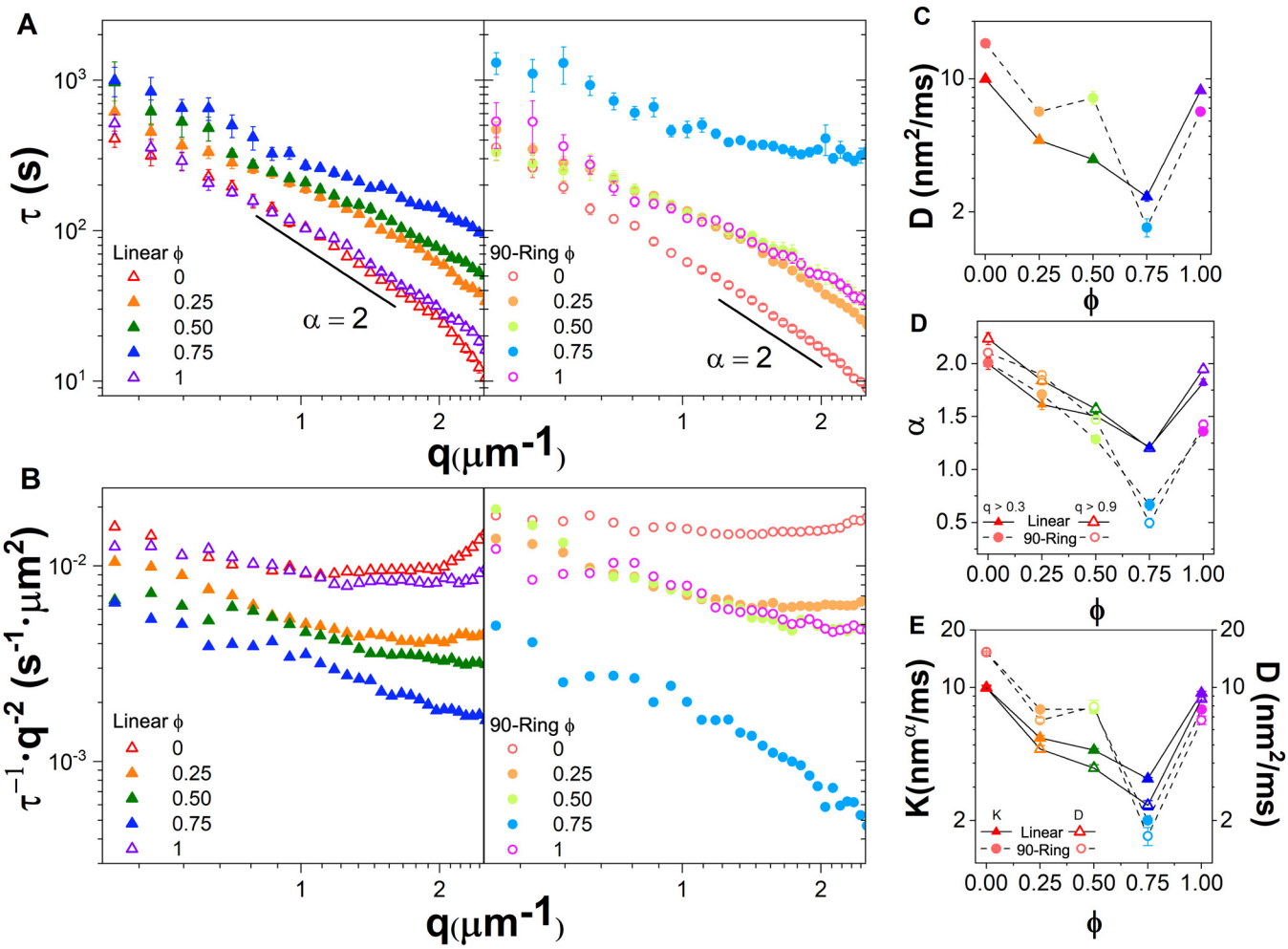

FIG. 3. Differential dynamic microscopy of DNA-dextran composites shows arrested dynamics and nonmonotonic dependence on the volume fraction of DNA. (a) Characteristic decay time τ versus wave vector q for DNA-dextran composites with linear DNA (left panel, triangles, dark shades) and 90-ring DNA (right panel, circles, light shades) at volume fractions of $\phi = 0$, $\phi = 0.25$, 0.5, 0.75, and 1, as indicated in the legend. Scaling bars indicate diffusive dynamics, i.e., $\tau(q) \sim q^{-2}$. (b) Data shown in (a) plotted as $\tau^{-1}q^{-2}$, which equates to a q-independent diffusion coefficient D for systems that exhibit normal diffusion. Increased negative slopes indicate more arrested or halted motion. (c) Diffusion coefficient versus ϕ for composites with 90-ring (circles, dashed connecting line) and linear (triangles, solid connecting line) DNA determined by fitting the data in (a) to $\tau(q) = 1/(Dq^2)$. (d) Transport scaling exponent α versus ϕ for composites with 90-ring (circles, dashed connecting line) and linear (triangles, solid connecting line) DNA determined from fitting the data in (a) to $\tau(q) = 1/(Kq^{\alpha})$. Fits are performed over the entire q range shown (filled symbols) and for $q > 0.9$ (open symbols). $q = 2$ signifies normal diffusion and $q \to 0$ indicates kinetic arrest. (e) Generalized transport coefficient K (left axis, filled symbols) compared to the corresponding diffusion coefficient D (right axis, open symbols) versus ϕ for composites with ring (circles, dashed connecting line) and linear (triangles, solid connecting line) DNA determined from fitting the data in (a) to $\tau(q) = 1/(Kq^{\alpha})$ or $\tau(q) = 1/(Dq^2)$. Error bars (many of which are too small to see) are determined from fits to the data.

Figure 3(a) shows the characteristic decorrelation times τ of diffusing DNA polymers versus wavenumber q, which we determine by fitting the radially averaged image structure function $D(q, \Delta t)$ to a stretched exponential, as described in Sec. II. In general, higher τ values for a given q indicate slower motion. By fitting $\tau(q)$ to the power-law function $\tau = 1/(Kq^{\alpha})$, one can determine the type of motion. Normal Brownian diffusion is described by $\alpha = 2$ with K equating to the corresponding diffusion coefficient D. We can, therefore, estimate diffusion coefficients for our data by fitting each curve to $\alpha = 2$ scaling [Fig. 3(c)]. Conversely, restricted or halted motion, such as in glassy systems, often results in much weaker q dependence ($\alpha \to 0$) as we see in some of the data [Fig. 3(d)] [96,97]. If α deviates from 2, then K is a generalized transport coefficient with dimensions that depend on α [Fig. 3(e)].

For both DNA topologies, transport is fastest (smallest τ) and scaling is closest to diffusive ($\alpha = 2$) in dextran solutions ($\phi = 0$) and is slowest and exhibits the weakest dependence in $\phi = 0.75$ composites. To better visualize the deviation from normal diffusion and the nonmonotonic ϕ dependence shown in Fig. 3(a), we plot $1/\tau q^2$ [Fig. 3(b)], which, for diffusive transport, is a horizontal line with a y-intercept equal to D [Fig. 3(c)]. Halted transport or kinetic arrest manifests as a negative slope approaching $\alpha - 2 \approx -2$, as seen for $\phi = 0.75$ 90-ring composites. Such kinetically arrested states, observed in simulations of entangled ring polymer solutions [31], indicate ring-ring and ring-linear threading events.

It may be possible that ring DNA is threaded by dextran polymers. However, the much smaller size of dextran polymers compared to DNA rings would limit their ability to halt ring diffusion by maintaining long-lived threadings. Indeed, as previously observed in ring-linear melts, interpenetration (i.e., threading) by short linear polymers (akin to the dextran used here) cause tracer rings to swell and diffuse faster than when in their own melts [54]. Dextran-mediated swelling at $\phi = 0.75$ could facilitate DNA-DNA threading events responsible for glassy behavior, by reducing the fraction of double-folded and collapsed rings [21].

These results corroborate our bulk rheology data that suggests that ring threadings are most pervasive and long-lived at $\phi = 0.75$. Conversely, $\phi = 1$ and 0.5 ring composites exhibit q-dependence that is in between diffusive and arrested ($\alpha \approx 1.4$) [Fig. 3(d)], indicative of contributions from populations of both diffusive entangled rings and halted threaded rings—as our rheology results suggest.

Linear DNA composites exhibit similar trends, with minimum α and D values at $\phi = 0.75$, followed by 0.5, but the variation in α with ϕ is much weaker [Figs. 3(c) and 3(d)]. This weaker ϕ-dependence for linear chains is more evident when we evaluate the generalized transport coefficients K for the different composites: K exhibits a weaker ϕ dependence for linear chains than the corresponding diffusion coefficient [Fig. 3(e)]. Further, the pure linear DNA solution exhibits diffusive scaling ($\alpha \approx 2$), in contrast to the 90-rings ($\alpha \approx 1.4$). These topology-dependent effects highlight the distinct relaxation mechanisms at play in the different composites. Namely, threading dominates 90-ring composites whereas depletion-driven DNA elongation and bundling mediate the restricted diffusion in linear DNA composites.

These different transport modes are expected to have different degrees of heterogeneity [39,115], which we evaluate by examining the spread in the ISFs generated from DDM performed on different ROIs in the time-series (Fig. S5) [120]. In general, the spreads in the ISFs for 90-ring composites are larger than that for linear composites, in line with simulations that show that entangled ring polymer solutions with glassy dynamics exhibit heterogeneous transport [30,31]. Moreover, considering the 90-ring composites at short lag times ($\Delta t \lesssim 100$ s), the spread in the ISFs for $\phi = 0.5$ and 1 is significantly broader than that for $\phi = 0.75$. This variation indicates that over small timescales the dynamics of the $\phi = 0.75$ composite is dominated by a single mechanism (i.e., long-lived threading), whereas for $\phi = 0.5$ and $\phi = 1$ composites, a combination of faster modes (i.e., short-lived threading, single-chain threading, modified reptation), not prevalent at $\phi = 0.75$, also contribute to the dynamics.

While threading alone, by rings or linear chains, is predicted to result in heterogeneous transport, this heterogeneity is predicted to increase as Δt increases [30]. At short lag times, below the average threading lifetime, there should be much less heterogeneity as all rings are kinetically arrested by threadings [30]. This effect is what we see for 90-rings in Fig. S5 [120]. Namely, $\phi = 0.75$ exhibits the broadest distribution of all ISFs for $\Delta t \gtrsim 200$ s, whereas the spreads in ISFs for $\phi = 0.5$ and $\phi = 1$ are much broader for $\Delta t \lesssim 200$ s. Importantly, delayed onset of heterogeneity, as we see for $\phi = 0.75$, is expected to be more pronounced when rings are threaded by multiple chains [30,34], which we expect to be the case in the $\phi = 0.75$ composite, in which swelling facilitates threading. In contrast, heterogeneity associated with a combination of single-threaded, multithreaded, and double-folded rings, as we expect for $\phi = 0.5$ and $\phi = 1$, should manifest more strongly at shorter lag times as the associated relaxation timescales are shorter.

Finally, we note that the scaling of $\tau(q)$ is weaker at smaller q values (i.e., longer lengthscales λ), as depicted by comparing α values computed over the entire q range ($q = 2\pi/\lambda \approx 0.3$–$2.5\,\mu\text{m}^{-1}$, $\lambda \approx 2.5 - 20\,\mu\text{m}$) to those excluding $q_c \lesssim 0.9\,\mu\text{m}^{-1}$($\lambda_c \gtrsim 7\,\mu\text{m}$) [Fig. 3(d)]. We can understand this effect and the corresponding lengthscale λ_c as arising from entanglements and threadings that hinder polymer motion beyond a few entanglement lengths l_e [39,116] such that restricted transport ($\alpha \to 0$) will be more apparent for $\lambda > \text{O}(l_e)$. Indeed, Fig. S3 [120] shows that the range of l_e values for the different composites span from $\sim$0.3 μm (for linear $\phi = 0.75$) to 20 μm (for ring $\phi = 0.25$), on the order of λ_c, corroborating this interpretation.

D. SMT to corroborate DDM and expand the spatiotemporal scales of transport measurements

To further understand the nonmonotonic dependence of transport and rheology on ϕ, and the ϕ-dependent differences between 90-ring and linear DNA, we perform SMT measurements of DNA in $\phi = 0.75$ and $\phi = 1$ composites.

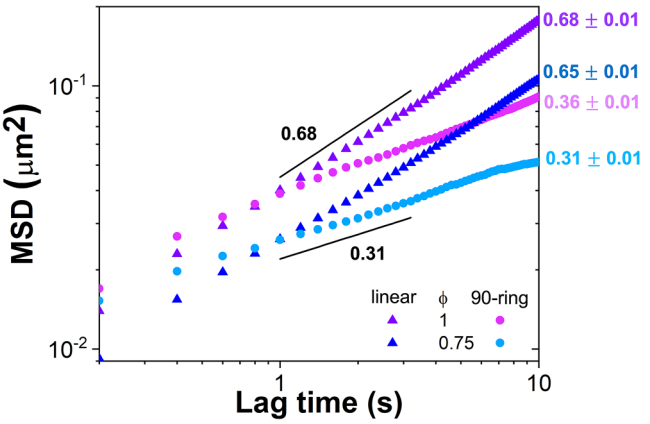

FIG. 4. Ring and linear DNA exhibit topology-dependent subdiffusion at high DNA volume fractions. *MSD* versus lag time Δt for linear (triangles) and 90-ring (circles) DNA diffusing in composites with DNA volume fractions of $\phi = 1$ and $\phi = 0.75$ (see legend). Black lines represent power-law scaling with exponents listed. The exponent β from fitting each curve to $MSD \sim \Delta t^{\beta}$ is listed to the right of each curve. In all cases, DNA exhibits subdiffusion ($\beta < 1$) with rings displaying greater deviation from normal diffusion ($\beta = 1$) than linear DNA. For both topologies *MSD*s are ∼2× lower in $\phi = 0.75$ composites compared to $\phi = 1$.

We focus on $\phi = 0.75$ as it deviates most strongly from normal diffusive scaling for both topologies. Figure 4 shows the center-of-mass *MSD* versus lag time Δt for ring and linear DNA at $\phi = 0.75$ and 1. All cases exhibit anomalous subdiffusion, i.e., $MSD \sim \Delta t^{\beta}$ where $\beta < 1$. For both ϕ values, rings display greater deviation from normal diffusion compared to linear DNA, with an average value of $\beta \simeq 0.34$ compared to ∼0.67 for linear chains.

These β values are comparable to, but slightly lower than, those previously reported for tracer ring and linear DNA molecules in networks of cytoskeleton filaments [39,113,116]. In those experiments, the lower β value for rings was attributed to threading by cytoskeleton filaments, further supporting our interpretation of the results shown in Figs. 2 and 3. Moreover, Chapman *et al.* [74] reported anomalous scaling exponents of $\beta \simeq 0.75$ and ∼0.72 for 11 and 115 kbp linear DNA in $\sim 10c^*$ dextran solutions for $\Delta t \lesssim 10$ s (the upper limit of our SMT measurements) after which normal diffusion is observed. These exponents are similar but higher than our SMT-measured $\beta \simeq 0.65$ for the $\phi = 0.75$ linear DNA composite, suggesting that DNA elongation is likely a principal contributor to the dynamics we measure, but that an additional contribution which would reduce the scaling exponent further, such as multifilament bundling, also plays an important role. Moreover, in contrast to [74], deviation from normal diffusion for the $\phi = 0.75$ linear case is evident in our DDM measurements, which span $\Delta t \simeq 10$–1000 s, further suggesting an additional slow contribution to the DNA relaxation.

Conversely, previous SMT experiments of tracer (i.e., $\phi = 0$) 115 kbp ring and linear DNA crowded by ∼4–14c^* dextran solutions reported normal diffusion for $\Delta t \gtrsim 10$ s [74,75]. This result, which aligns with our DDM measurements ($\Delta t \simeq 10 - 1000$ s) for $\phi = 0$ (Fig. 3), supports our conclusions that (i) threading by dextran does not contribute to the phenomena we report here for 90-rings and (ii) bundling of linear DNA (not seen in [74,75]) plays a key role in the observed subdiffusion of linear DNA in composites above a critical fraction of DNA, in particular, at longer lag times. Depletion-driven elongation of linear DNA, as reported in [74,75], likely facilitates nematic DNA bundling, by extending DNA from random coil configurations to extended conformations similar to those of semiflexible polymers such as actin filaments. Further, previous studies on entangled actin solutions [117,118] have reported similar subdiffusive β exponents to those for our linear DNA composites, supporting our interpretation that bundling, which serves to stiffen the DNA (i.e., increasing l_k), underlies the hindered diffusion and increased elasticity of linear DNA-dextran composites compared to $\phi = 1$ DNA solutions.

We further point out that β is slightly lower (outside of measured error) for $\phi = 0.75$ compared to $\phi = 1$ for both topologies, and the value of the *MSD* at a given Δt is ∼2-fold lower, in line with our DDM and bulk rheology data. The strongly anomalous diffusion and concomitantly low *MSD* for 90-rings at $\phi = 0.75$ corroborate our interpretation of glassy dynamics due to ring-ring and ring-linear threadings that pin rings in kinetically arrested states. Further, as such glassy dynamics are predicted to be accompanied by heterogeneous transport, we evaluate the van Hove displacement distributions from our SMT measurements for lag times $\Delta t = 1 - 15$ s (see Fig. S6) [120], which span the first decade of DDM lag times shown in Fig. S5 [120]. The distributions display non-Gaussian exponential tails, similar to those reported in [30], that indicate heterogeneous transport. The composites with the most non-Gaussian distributions correlate with those that show the most spread in the ISFs for $\Delta t < 40$ s (i.e., $\phi = 1$ for ring and linear DNA) (see Fig. S5) [120]. For larger Δt (>100 s), outside our SMT measurement range, we expect the trend to flip such that the $\phi = 0.75$ composites, which display the widest spreads in ISFs for $\Delta t > 100$ s, exhibit the most pronounced non-Gaussianity.

Finally, as we discuss above, the timescale probed by SMT is lower than for DDM [Fig. 1(b)], corresponding to $\omega \simeq 0.6 - 30$ rad/s. In this range, the linear DNA solution ($\phi = 1$) exhibits more elastic-like behavior compared to the lower frequencies probed by DDM, in which it exhibits terminal flow behavior. As such, DDM measurements show $\phi = 1$ linear DNA obeying normal Brownian diffusion ($\alpha \approx 2$), while SMT experiments measure subdiffusive transport.

E. Coupling bulk rheological properties to macromolecular dynamics

To quantitatively compare and couple bulk and molecular-level dynamics, we compare the diffusion coefficient determined from DDM [Fig. 3(c)] to the zero-shear viscosity measured via bulk rheology [Fig. 2(e)]. In Newtonian fluids (as well as some non-Newtonian fluids), these quantities are inversely related via the Stokes–Einstein fluctuation-dissipation relation such that D versus η_0^{-1} should exhibit linear scaling, provided the size and conformation of the polymers are not changing. As shown in Fig. 5(a), we find that, in general, higher diffusion coefficients are coupled to lower viscosities, as we may expect.

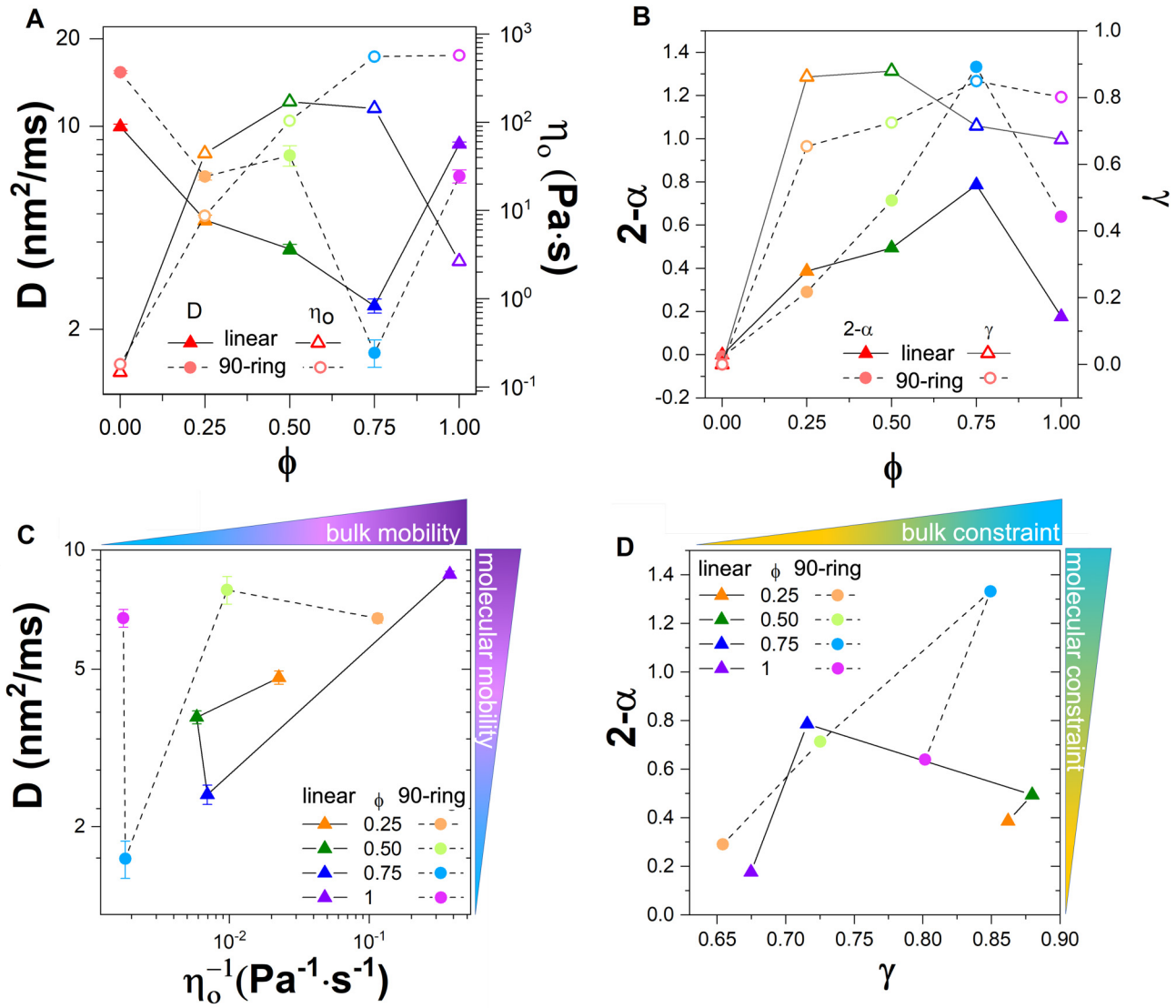

FIG. 5. Coupling of bulk and molecular-level metrics reveals emergent scale-dependent dynamics in DNA-dextran composites. (a) Diffusion coefficient D determined from DDM (left axis, closed symbols) and zero-shear viscosity η_0 (right axis, open symbols) determined via bulk rheology for DNA-dextran composites with linear (triangles) or 90-ring (circles) DNA at varying DNA volume fractions ϕ. (b) Deviation from diffusive DDM scaling, quantified by 2-α (left axis, closed symbols), and complex viscosity thinning exponent γ (right axis, open symbols) determined via bulk rheology versus ϕ for DNA-dextran composites with linear (triangles) and ring (circles) DNA. (c) Data shown in (a) plotted as D versus η_0^{-1} for DNA-dextran composites with 90-ring (circles, dashed connecting line) and linear (triangles, solid connecting line) DNA. Both quantities are measures of mobility with larger values indicating higher mobility, as indicated by the gradients. (d) Data shown in (b) plotted as 2-α versus γ for DNA-dextran composites with ring (circles, dashed connecting line) and linear (triangles, solid connecting line) DNA. Both quantities are indicators of steric constraints with larger values indicating more constrained dynamics, as indicated by the gradients.

To better visualize and quantify the relation between D and η_0^{-1}, which are measures of mobility on the molecular scale and bulk scale, respectively, we plot the phase map of (D, η_0^{-1}) combinations [Fig. 5(c)]. Data points in the lower-left and upper-right of the plot correspond to nearly immobile and highly mobile systems, respectively, across scales. It is clear that the $\phi = 0.75$ ring composite is the least mobile and the $\phi = 1$ linear DNA is the most mobile across all scales. Conversely, data points that are aligned horizontally or vertically indicate systems in which mobility only appears to change at the bulk or molecular scale, respectively. For example, 90-ring composites with $\phi = 0.25$, 0.5 and 1 have nearly identical diffusion coefficients, yet the corresponding η_0^{-1} values increase by 2 orders of magnitude as ϕ increases. This result suggests that similar molecular-scale mechanisms dictate the diffusion of individual DNA molecules across the different composites; however, the bulk mobility increases as ϕ increases.

In Fig. 5(b), we examine the bulk complex viscosity thinning exponent γ and the deviation of the DDM transport coefficient from diffusive dynamics, which we define as the quantity 2-α, as a function of ϕ [Fig. 5(b)]. Both metrics quantify constraint, with γ ranging from 0 for Newtonian fluids to 1 for highly entangled or threaded systems and 2-α spanning from 0 for normal Brownian diffusion to 2 for arrested dynamics. As such, we expect the dependence of γ and 2-α on ϕ and topology to track with one another, corresponding to data points populating the lower-left (minimal

constraints) and upper-right (many constraints) of the phase map shown in Fig. 5(d). This relationship loosely holds for many of the composites, with the $\phi = 0.75$ 90-ring composite appearing the most constrained (top-right) and the $\phi = 1$ linear composite exhibiting negligible constraints (bottom-left) across all scales. However, we also find cases, such as $\phi = 0.25$ and 0.5 linear DNA composites, that appear highly entangled and constrained at the bulk scale (righthand side of the plot), while displaying relatively little deviation from diffusive scaling at the molecular scale (bottom portion of the plot).

Finally, the data in Figs. 5(c) and 5(d) show that $\phi = 0.25$ linear DNA composites have increased bulk η_0 and γ values and reduced microscale D and α values compared to $\phi = 1$ linear DNA solutions, while the opposite is true of all metrics for 90-rings. We understand this effect as arising from the loss of DNA-DNA threadings which, when present, lead to kinetically arrested states that suppress bulk dissipation. Further, dextran solutions at sufficiently high volume fractions (comparable to $\phi \leq 0.5$ composites) have been shown to compact ring DNA, which would serve to reduce entanglements with neighbors at low DNA concentration. Indeed, we show that l_e for rings at $\phi = 0.25$ is greater than the DNA contour length L and greater than that computed assuming $l_e \sim \phi^{-1}$ scaling, indicating that compaction and reduced entanglements dictate ring dynamics at low ϕ. Conversely, recent work demonstrates that rings are swollen by transient threading of linear polymers that are below the entanglement threshold (such as in our high ϕ composites) [54]. This swelling promotes entanglements and threading by linear chains, which likewise facilitates thinning [Fig. 2(f)]. As such, we argue that rings switching between compacted and swollen states underlies the phenomenon that the diffusion coefficient D is lower, and the zero-shear viscosity η_0 and thinning exponent γ are higher, for linear versus 90-ring DNA composites at $0 \leq \phi \leq 0.5$, whereas rings become slower and exhibit enhanced bulk viscosity and thinning compared their linear counterparts beyond $\phi = 0.5$.

These emergent regions of the phase space indicate that composites can exhibit scale-dependent dynamics tuned by the relative concentrations of DNA and dextran as well as the DNA topology. These data also demonstrate the need for coupled microscale and bulk measurement methods to shed light on the physics underlying the rheology and transport properties that complex systems manifest. A final example to demonstrate this point is the apparent discrepancy between D measured via DDM and τ_D measured via bulk rheology for $\phi = 1$ linear DNA. For entangled linear polymers, $\tau_D \approx L_0^2/D$, where $L_0 \approx (L/l_e)a$ is the primitive path length of an entangled polymer [8]. For our linear DNA solution, we measure $D \approx 9\,\mathrm{nm}^2/\mathrm{ms}$ via DDM, within a factor of 2 of the value measured previously with SMT [88]. Using this value gives $\tau_{D,micro} \approx 920\,\mathrm{s}$, which is substantially larger than $\tau_{D,bulk} \approx 25\,\mathrm{s}$ measured via bulk rheology. However, because our entanglement density of $Z \approx L/l_e \approx 10$ [determined from G_N^0, see Fig. S3 [120] and Fig. 2(d)] is well below $O(10^2)$, we cannot ignore contour length fluctuations (CLFs), i.e., fluctuations in the length of the primitive path, which reduce the disengagement time [8]. Specifically, CLF contributions are predicted to reduce τ_D according to the relation $\tau_D^{(CLF)} \approx \tau_D\left(1 - (X/\sqrt{Z})\right)^2$ where X is a numerical factor that is of order unity and predicted to be greater than ~1.5 [8,119]. Using $\tau_D^{(CLF)} \approx \tau_{D,bulk} \approx 25\,\mathrm{s}$ and $\tau_D \approx \tau_{D,micro} \approx 920\,\mathrm{s}$, we compute $X \approx 2.6$, which is indeed of order unity and >1.5. Thus, not only do our bulk and molecular-level measurements align with one another, but, taken together, they demonstrate the significance of CLF contributions to entangled chain dynamics and shed light on the numerical factor that relates the two for entangled DNA.

IV. CONCLUSIONS

In summary, we have coupled bulk rheology measurements with fluorescence imaging and DDM analysis to directly correlate the bulk viscoelastic properties of entangled DNA-dextran composites to the corresponding microscale polymer transport (Fig. 1). Importantly, we performed both measurements—at lengthscales that differ by ~4 orders of magnitude—on the exact same samples, under the same conditions, and within minutes of each other. In this way, we explicitly connect macroscopic rheological properties to the underlying macromolecular dynamics (Fig. 5).

We show that DNA-dextran composites exhibit topology-dependent nonmonotonic dependences of bulk rheological properties and macromolecular transport properties on the fraction of DNA comprising the composites. We attribute this emergent behavior to the different ways that dextran polymers alter the conformation and self-association of ring and linear DNA via depletion interactions. Rings may be either compacted (at $\phi \leq 0.5$) or swollen (at $\phi = 0.75$) by dextran. When swollen, threadings by neighboring ring and linear DNA give rise to near kinetic arrest. For linear DNA, depletion-driven stretching and bundling of the DNA may either reduce connectivity (at low ϕ) or give rise to overlapping extended bundles of DNA with properties akin to semiflexible polymers (at high ϕ).

It is intriguing that such stark DNA topology dependence across scales could be driven by dextran polymers with $R_g \simeq 19\,\mathrm{nm}$, an order of magnitude smaller than $R_g(\gtrsim 280\,\mathrm{nm})$, $l_k(\gtrsim 100\,\mathrm{nm})$ and $l_e(\gtrsim 300\,\mathrm{nm})$ for the DNA, preventing individual dextran polymers to differentiate between the two possible topologies of a neighboring DNA strand. Instead, it is the collective action of dextran polymers seeking to maximize their available volume (and thus entropy) that leads to the topology-dependent phenomena we report. We can qualitatively understand this effect in the following way.

One mechanism that short dextran polymers can use to increase their available volume in solution is to interpenetrate the DNA random coils. This interpenetration causes rings, with no free ends, to swell from random coil configurations to more open ring conformations to reduce excluded volume within the coil [54]. Alternatively, dextran volume maximization can induce the compaction of rings [75]. However, compaction is more energetically unfavorable for the DNA, as it forces repelling DNA segments to be in close vicinity. Only when the dextran concentration is high enough, does the entropic gain from dextran volume maximization outweigh

the energetic cost to collapse the DNA. At even higher dextran concentrations, we may expect aggregation of compacted rings to further minimize dextran excluded volume, analogous to the formation of bundles of linear DNA. In the opposite limit, at lower dextran concentrations, and thus higher DNA concentrations, the threading of rings by linear DNA and other rings, facilitated by dextran-mediated swelling, is more probable and would counteract the drive toward compaction.

Conversely, for linear DNA, that does have free ends, interpenetration of a random coil by dextran drives a DNA strand to entropically stretch into an elongated structure, rather than a swollen open ring, to minimize the volume excluded to the dextran. Bundling of elongated linear DNA, which would further minimize excluded volume, is energetically unfavorable and requires DNA strands to come into close contact with one another, which is highly improbable at tracer DNA concentrations ($\phi = 0$), but becomes possible as ϕ increases. As such, the maximal elasticity at $\phi = 0.75$ for linear DNA arises because the DNA concentration is high enough such that bundling can occur without destroying network connectivity.

More generally, our results demonstrate that for polymer composites, the whole is not always equal to the sum of its parts, rather mixing polymers with distinct structures, sizes, and topologies can give rise to emergent dynamics that can either span from microscopic to macroscopic scales or display scale-dependence depending on the composite composition. We further show that polymer end-closure plays an important role in interactions between the different species comprising the composites, with ring polymers conferring uniquely suppressed dissipation and relaxation.

ACKNOWLEDGMENTS

We acknowledge Maya Nugent for her help in preparing figures and acknowledge funding from an AFOSR award (Nos. FA9550-17-1-0249 and FA9550-21-1-0361) to R.M.R.-A. and an NSF CBET award (No. CBET-1919429) to R.M. (PI) and RMRA (co-PI).

AUTHOR DECLARATIONS

Conflict of Interest

The authors have no conflicts to disclose.

REFERENCES

[1] Cremer, T., and C. Cremer, "Chromosome territories, nuclear architecture and gene regulation in mammalian cells," Nat. Rev. Genet. **2**, 292–301 (2001).

[2] Meaburn, K. J., and T. Misteli, "Chromosome territories," Nature **445**, 379–381 (2007).

[3] van Loenhout, M. T. J., M. V. de Grunt, and C. Dekker, "Dynamics of DNA supercoils," Science **338**, 94–97 (2012).

[4] Yamamoto, T., and Y. Tezuka, "Topological polymer chemistry: A cyclic approach toward novel polymer properties and functions," Polym. Chem. **2**, 1930–1941 (2011).

[5] Zhu, Y., and N. S. Hosmane, "Advanced developments in cyclic polymers: Synthesis, applications, and perspectives," ChemistryOpen **4**, 408–417 (2015).

[6] Golba, B., E. M. Benetti, and B. G. De Geest, "Biomaterials applications of cyclic polymers," Biomaterials **267**, 120468 (2021).

[7] De Gennes, P. G., *Scaling Concepts in Polymer Physics* (Cornell University, Ithaca, 1979).

[8] Doi, M., and S. F. Edwards, *The Theory of Polymer Dynamics* (Clarendon, New York, 1986).

[9] McLeish, T., "Polymers without beginning or end," Science **297**, 2005–2006 (2002).

[10] McLeish, T., "Floored by the rings," Nat. Mater. **7**, 933–935 (2008).

[11] Abadi, M., M. F. Serag, and S. Habuchi, "Entangled polymer dynamics beyond reptation," Nat. Commun. **9**, 5098 (2018).

[12] Vlassopoulos, D., R. Pasquino, and F. Snijkers, *Topological Polymer Chemistry* (World Scientific, Singapore, 2012), pp. 291–316.

[13] Richter, D., S. Gooßen, and A. Wischnewski, "Celebrating soft matter's 10th anniversary: Topology matters: Structure and dynamics of ring polymers," Soft Matter **11**, 8535–8549 (2015).

[14] Hou, J.-X., "Stress relaxation of entangled ring polymer chains in a linear matrix," J. Rheol. **64**, 1315–1324 (2020).

[15] Regan, K., S. Ricketts, and R. Robertson-Anderson, "DNA as a model for probing polymer entanglements: Circular polymers and non-classical dynamics," Polymers **8**, 336 (2016).

[16] Peddireddy, K. R., M. Lee, C. M. Schroeder, and R. M. Robertson-Anderson, "Viscoelastic properties of ring-linear DNA blends exhibit nonmonotonic dependence on blend composition," Phys. Rev. Res. **2**, 023213 (2020).

[17] Doi, Y., A. Matsumoto, T. Inoue, T. Iwamoto, A. Takano, Y. Matsushita, Y. Takahashi, and H. Watanabe, "Re-examination of terminal relaxation behavior of high-molecular-weight ring polystyrene melts," Rheol. Acta **56**, 567–581 (2017).

[18] Yan, Z.-C., S. Costanzo, Y. Jeong, T. Chang, and D. Vlassopoulos, "Linear and nonlinear shear rheology of a marginally entangled ring polymer," Macromolecules **49**, 1444–1453 (2016).

[19] Parisi, D., M. Kaliva, S. Costanzo, Q. Huang, P. J. Lutz, J. Ahn, T. Chang, M. Rubinstein, and D. Vlassopoulos, "Nonlinear rheometry of entangled polymeric rings and ring-linear blends," J. Rheol. **65**, 695–711 (2021).

[20] Parisi, D., S. Costanzo, Y. Jeong, J. Ahn, T. Chang, D. Vlassopoulos, J. D. Halverson, K. Kremer, T. Ge, M. Rubinstein, G. S. Grest, W. Srinin, and A. Y. Grosberg, "Nonlinear shear rheology of entangled polymer rings," Macromolecules **54**, 2811–2827 (2021).

[21] Smrek, J., K. Kremer, and A. Rosa, "Threading of unconcatenated ring polymers at high concentrations: Double-folded vs time-equilibrated structures," ACS Macro Lett. **8**, 155–160 (2019).

[22] Michieletto, D., "On the tree-like structure of rings in dense solutions," Soft Matter **12**, 9485–9500 (2016).

[23] McLeish, T. C. B., "Tube theory of entangled polymer dynamics," Adv. Phys. **51**, 1379–1527 (2002).

[24] Rubinstein, M., "Dynamics of ring polymers in the presence of fixed obstacles," Phys. Rev. Lett. **57**, 3023–3026 (1986).

[25] Kapnistos, M., M. Lang, D. Vlassopoulos, W. Pyckhout-Hintzen, D. Richter, D. Cho, T. Chang, and M. Rubinstein, "Unexpected power-law stress relaxation of entangled ring polymers," Nat. Mater. **7**, 997–1002 (2008).

[26] Parisi, D., J. Ahn, T. Chang, D. Vlassopoulos, and M. Rubinstein, "Stress relaxation in symmetric ring-linear polymer blends at Low ring fractions," Macromolecules **53**, 1685–1693 (2020).

[27] Doi, Y., A. Takano, Y. Takahashi, and Y. Matsushita, "Melt rheology of tadpole-shaped polystyrenes with different ring sizes," Soft Matter **16**, 8720–8724 (2020).

[28] Huang, Q., J. Ahn, D. Parisi, T. Chang, O. Hassager, S. Panyukov, M. Rubinstein, and D. Vlassopoulos, "Unexpected stretching of entangled ring macromolecules," Phys. Rev. Lett. **122**, 208001 (2019).

[29] Smrek, J., I. Chubak, C. N. Likos, and K. Kremer, "Active topological glass," Nat. Commun. **11**, 1–11 (2020).

[30] Michieletto, D., N. Nahali, and A. Rosa, "Glassiness and heterogeneous dynamics in dense solutions of ring polymers," Phys. Rev. Lett. **119**, 197801 (2017).

[31] Michieletto, D., and M. S. Turner, "A topologically driven glass in ring polymers," Proc. Natl. Acad. Sci. U.S.A. **113**, 5195–5200 (2016).

[32] Smrek, J., and A. Y. Grosberg, "Understanding the dynamics of rings in the melt in terms of the annealed tree model," J. Phys.: Condens. Matter **27**, 064117 (2015).

[33] Brás, A. R., R. Pasquino, T. Koukoulas, G. Tsolou, O. Holderer, A. Radulescu, J. Allgaier, V. G. Mavrantzas, W. Pyckhout-Hintzen, A. Wischnewski, D. Vlassopoulos, and D. Richter, "Structure and dynamics of polymer rings by neutron scattering: Breakdown of the rouse model," Soft Matter **7**, 11169–11176 (2011).

[34] Tsalikis, D. G., V. G. Mavrantzas, and D. Vlassopoulos, "Analysis of slow modes in ring polymers: Threading of rings controls long-time relaxation," ACS Macro Lett. **5**, 755–760 (2016).

[35] Katsarou, A., A. Tsamopoulos, D. Tsalikis, and V. Mavrantzas, "Dynamic heterogeneity in ring-linear polymer blends," Polymers **12**, 752 (2020).

[36] Halverson, J. D., G. S. Grest, A. Y. Grosberg, and K. Kremer, "Rheology of ring polymer melts: From linear contaminants to ring-linear blends," Phys. Rev. Lett. **108**, 038301 (2012).

[37] Kong, D., S. Banik, M. J. San Francisco, M. Lee, R. M. Robertson Anderson, C. M. Schroeder, and G. B. McKenna, "Rheology of entangled solutions of ring–linear DNA blends," Macromolecules **55**, 1205–1217 (2022).

[38] Smrek, J., J. Garamella, R. Robertson-Anderson, and D. Michieletto, "Topological tuning of DNA mobility in entangled solutions of supercoiled plasmids," Sci. Adv. **7**, eabf9260 (2021).

[39] Wulstein, D. M., K. E. Regan, J. Garamella, R. J. McGorty, and R. M. Robertson-Anderson, "Topology-dependent anomalous dynamics of ring and linear DNA are sensitive to cytoskeleton crosslinking," Sci. Adv. **5**, eaay5912 (2019).

[40] Zhou, Y., C. D. Young, M. Lee, S. Banik, D. Kong, G. B. McKenna, R. M. Robertson-Anderson, C. E. Sing, and C. M. Schroeder, "Dynamics and rheology of ring-linear blend semidilute solutions in extensional flow: Single molecule experiments," J. Rheol. **65**, 729–744 (2021).

[41] Hsiao, K.-W., C. M. Schroeder, and C. E. Sing, "Ring polymer dynamics are governed by a coupling between architecture and hydrodynamic interactions," Macromolecules **49**, 1961–1971 (2016).

[42] Robertson, R. M., and D. E. Smith, "Strong effects of molecular topology on diffusion of entangled DNA molecules," Proc. Natl. Acad. Sci. U.S.A. **104**, 4824–4827 (2007).

[43] Tsalikis, D. G., and V. G. Mavrantzas, "Threading of ring poly(ethylene oxide) molecules by linear chains in the melt," ACS Macro Lett. **3**, 763–766 (2014).

[44] Papadopoulos, G., D. Tsalikis, and V. Mavrantzas, "Microscopic dynamics and topology of polymer rings immersed in a host matrix of longer linear polymers: Results from a detailed molecular dynamics simulation study and comparison with experimental data," Polymers **8**, 283 (2016).

[45] Michieletto, D., D. Marenduzzo, E. Orlandini, and M. Turner, "Ring polymers threadings, knot electrophoresis and topological glasses," Polymers **9**, 349 (2017).

[46] Teixeira, R. E., A. K. Dambal, D. H. Richter, E. S. G. Shaqfeh, and S. Chu, "The individualistic dynamics of entangled DNA in solution," Macromolecules **40**, 2461–2476 (2007).

[47] Chapman, C. D., K. Lee, D. Henze, D. E. Smith, and R. M. Robertson-Anderson, "Onset of Non-continuum effects in microrheology of entangled polymer solutions," Macromolecules **47**, 1181–1186 (2014).

[48] Roovers, J., "Viscoelastic properties of polybutadiene rings," Macromolecules **21**, 1517–1521 (1988).

[49] McKenna, G. B., B. J. Hostetter, N. Hadjichristidis, L. J. Fetters, and D. J. Plazek, "A study of the linear viscoelastic properties of cyclic polystyrenes using creep and recovery measurements," Macromolecules **22**, 1834–1852 (1989).

[50] Chapman, C. D., S. Shanbhag, D. E. Smith, and R. M. Robertson-Anderson, "Complex effects of molecular topology on diffusion in entangled biopolymer blends," Soft Matter **8**, 9177–9182 (2012).

[51] Zhou, Y., K.-W. Hsiao, K. E. Regan, D. Kong, G. B. McKenna, R. M. Robertson-Anderson, and C. M. Schroeder, "Effect of molecular architecture on ring polymer dynamics in semidilute linear polymer solutions," Nat. Commun. **10**, 1753 (2019).

[52] Tu, M. Q., M. Lee, R. M. Robertson-Anderson, and C. M. Schroeder, "Direct observation of ring polymer dynamics in the flow-gradient plane of shear flow," Macromolecules **53**, 9406–9419 (2020).

[53] S. Gooßen, M. Krutyeva, M. Sharp, A. Feoktystov, J. Allgaier, W. Pyckhout-Hintzen, A. Wischnewski and D. Richter. Sensing polymer chain dynamics through ring topology: A neutron spin echo study. Phys. Rev. Lett., **115**, 148302 (2015).

[54] Tsalikis, D. G., and V. G. Mavrantzas, "Size and diffusivity of polymer rings in linear polymer matrices: The key role of threading events," Macromolecules **53**, 803–820 (2020).

[55] Halverson, J. D., W. B. Lee, G. S. Grest, A. Y. Grosberg, and K. Kremer, "Molecular dynamics simulation study of nonconcatenated ring polymers in a melt. II. Dynamics," J. Chem. Phys. **134**, 204905 (2011).

[56] Peddireddy, K. R., D. Michieletto, G. Aguirre, J. Garamella, P. Khanal, and R. M. Robertson-Anderson, "DNA conformation dictates strength and flocculation in DNA–microtubule composites," ACS Macro Lett. **10**, 1540–1548 (2021).

[57] Francis, M. L., S. N. Ricketts, L. Farhadi, M. J. Rust, M. Das, J. L. Ross, and R. M. Robertson-Anderson, "Non-monotonic dependence of stiffness on actin crosslinking in cytoskeleton composites," Soft Matter **15**, 9056–9065 (2019).

[58] Ricketts, S. N., J. L. Ross, and R. M. Robertson-Anderson, "Co-entangled actin-microtubule composites exhibit tunable stiffness and power-law stress relaxation," Biophys. J. **115**, 1055–1067 (2018).

[59] Sheung, J. Y., D. H. Achiriloaie, C. Currie, K. Peddireddy, A. Xie, J. Simon-Parker, G. Lee, M. J. Rust, M. Das, J. L. Ross, and R. M. Robertson-Anderson, "Motor-driven restructuring of cytoskeleton composites leads to tunable time-varying elasticity," ACS Macro Lett. **10**, 1151–1158 (2021).

[60] Michieletto, D., R. Fitzpatrick, and R. M. Robertson-Anderson, "Maximally stiffening composites require maximally coupled rather than maximally entangled polymer species," Soft Matter **15**, 6703–6717 (2019).

[61] Jensen, M. H., E. J. Morris, R. D. Goldman, and D. A. Weitz, "Emergent properties of composite semiflexible biopolymer networks," BioArchitecture **4**, 138–143 (2014).

[62] Zribi, O. V., H. Kyung, R. Golestanian, T. B. Liverpool, and G. C. L. Wong, "Condensation of DNA-actin polyelectrolyte mixtures driven by ions of different valences," Phys. Rev. E **73**, 031911 (2006).

[63] Kobayashi, Y., Y. Doi, S. S. Abdul Rahman, E. Kim, T.-H. Kim, A. Takano, and Y. Matsushita, "SANS study of ring topology effects on the miscibility of polymer blends," Macromolecules **51**, 1885–1893 (2018).

[64] Sakaue, T., and C. H. Nakajima, "Miscibility phase diagram of ring-polymer blends: A topological effect," Phys. Rev. E **93**, 042502 (2016).

[65] Negishi, M., T. Sakaue, K. Takiguchi, and K. Yoshikawa, "Cooperation between giant DNA molecules and actin filaments in a microsphere," Phys. Rev. E **81**, 051921 (2010).

[66] Perry, S. L., "Phase separation: Bridging polymer physics and biology," Curr. Opin. Colloid Interface Sci. **39**, 86–97 (2019).

[67] Farhadi, L., S. N. Ricketts, M. J. Rust, M. Das, R. M. Robertson-Anderson, and J. L. Ross, "Actin and microtubule crosslinkers tune mobility and control co-localization in a composite cytoskeletal network," Soft Matter **16**, 7191–7201 (2020).

[68] Fitzpatrick, R., D. Michieletto, K. R. Peddireddy, C. Hauer, C. Kyrillos, B. J. Gurmessa, and R. M. Robertson-Anderson, "Synergistic interactions between DNA and actin trigger emergent viscoelastic behavior," Phys. Rev. Lett. **121**, 257801 (2018).

[69] Shim, Y. H., K. E. Lee, T. J. Shin, S. O. Kim, and S. Y. Kim, "Tailored colloidal stability and rheological properties of graphene oxide liquid crystals with polymer-induced depletion attractions," ACS Nano **12**, 11399–11406 (2018).

[70] Park, N., V. Rathee, D. L. Blair, and J. C. Conrad, "Contact networks enhance shear thickening in attractive colloid-polymer mixtures," Phys. Rev. Lett. **122**, 228003 (2019).

[71] González García, Á., M. M. B. Nagelkerke, R. Tuinier, and M. Vis, "Polymer-mediated colloidal stability: On the transition between adsorption and depletion," Adv. Colloid Interface Sci. **275**, 102077 (2020).

[72] Bocharova, V., A.-C. Genix, J.-M. Y. Carrillo, R. Kumar, B. Carroll, A. Erwin, D. Voylov, A. Kisliuk, Y. Wang, B. G. Sumpter, and A. P. Sokolov, "Addition of short polymer chains mechanically reinforces glassy poly(2-vinylpyridine)–silica nanoparticle nanocomposites," ACS Appl. Nano Mater. **3**, 3427–3438 (2020).

[73] Tuinier, R., T.-H. Fan, and T. Taniguchi, "Depletion and the dynamics in colloid–polymer mixtures," Curr. Opin. Colloid Interface Sci. **20**, 66–70 (2015).

[74] Chapman, C. D., S. Gorczyca, and R. M. Robertson-Anderson, "Crowding induces complex ergodic diffusion and dynamic elongation of large DNA molecules," Biophys. J. **108**, 1220–1228 (2015).

[75] Gorczyca, S. M., C. D. Chapman, and R. M. Robertson-Anderson, "Universal scaling of crowding-induced DNA mobility is coupled with topology-dependent molecular compaction and elongation," Soft Matter **11**, 7762–7768 (2015).

[76] O'Connor, T. C., T. Ge, M. Rubinstein, and G. S. Grest, "Topological linking drives anomalous thickening of ring polymers in weak extensional flows," Phys. Rev. Lett. **124**, 027801 (2020).

[77] Pelletier, V., N. Gal, P. Fournier, and M. L. Kilfoil, "Microrheology of microtubule solutions and actin-microtubule composite networks," Phys. Rev. Lett. **102**, 188303 (2009).

[78] Das, M., and F. C. MacKintosh, "Poisson's ratio in composite elastic media with rigid rods," Phys. Rev. Lett. **105**, 138102 (2010).

[79] Lin, Y.-C., G. H. Koenderink, F. C. MacKintosh, and D. A. Weitz, "Control of non-linear elasticity in F-actin networks with microtubules," Soft Matter **7**, 902–906 (2011).

[80] Buchanan, M., M. Atakhorrami, J. F. Palierne, and C. F. Schmidt, "Comparing macrorheology and one- and two-point microrheology in wormlike micelle solutions," Macromolecules **38**, 8840–8844 (2005).

[81] Del Giudice, F., M. Tassieri, C. Oelschlaeger, and A. Q. Shen, "When microrheology, bulk rheology, and microfluidics meet: Broadband rheology of hydroxyethyl cellulose water solutions," Macromolecules **50**, 2951–2963 (2017).

[82] Squires, T. M., and T. G. Mason, "Fluid mechanics of microrheology," Annu. Rev. Fluid Mech. **42**, 413–438 (2010).

[83] Schmidt, F. G., B. Hinner, and E. Sackmann, "Microrheometry underestimates the values of the viscoelastic moduli in measurements on F-actin solutions compared to macrorheometry," Phys. Rev. E **61**, 5646–5653 (2000).

[84] Weigand, W. J., A. Messmore, J. Tu, A. Morales-Sanz, D. L. Blair, D. D. Deheyn, J. S. Urbach, R. M. Robertson-Anderson, and K. Garikipati, "Active microrheology determines scale-dependent material properties of *Chaetopterus mucus*," PLoS One **12**, e0176732 (2017).

[85] Mason, T. G., K. Ganesan, J. H. van Zanten, D. Wirtz, and S. C. Kuo, "Particle tracking microrheology of complex fluids," Phys. Rev. Lett. **79**, 3282–3285 (1997).

[86] Robertson, R. M., and D. E. Smith, "Self-diffusion of entangled linear and circular DNA molecules: dependence on length and concentration," Macromolecules **40**, 3373–3377 (2007).

[87] Laib, S., R. M. Robertson, and D. E. Smith, "Preparation and characterization of a set of linear DNA molecules for polymer physics and rheology studies," Macromolecules **39**, 4115–4119 (2006).

[88] Robertson, R. M., S. Laib, and D. E. Smith, "Diffusion of isolated DNA molecules: Dependence on length and topology," Proc. Natl. Acad. Sci. U.S.A. **103**, 7310–7314 (2006).

[89] Sambrook, J., E. F. Fritsch, and T. Maniatis, *Molecular Cloning a Laboratory Manual* (Cold Spring Harbor Laboratory, New York, 1989).

[90] Peddireddy, K. R., M. Lee, Y. Zhou, S. Adalbert, S. Anderson, C. M. Schroeder, and R. M. Robertson-Anderson, "Unexpected entanglement dynamics in semidilute blends of supercoiled and ring DNA," Soft Matter **16**, 152–161 (2020).

[91] Jones, J. J., J. R. C. van der Maarel, and P. S. Doyle, "Effect of nanochannel geometry on DNA structure in the presence of macromolecular crowding agent," Nano Lett. **11**, 5047–5053 (2011).

[92] Aime, S., and L. Cipelletti, "Probing shear-induced rearrangements in Fourier space. II. Differential dynamic microscopy," Soft Matter **15**, 213–226 (2019).

[93] Philippe, A., S. Aime, V. Roger, R. Jelinek, G. Prévot, L. Berthier, and L. Cipelletti, "An efficient scheme for sampling fast dynamics at a low average data acquisition rate," J. Phys.: Condens. Matter **28**, 075201 (2016).

[94] He, K., F. Babaye Khorasani, S. T. Retterer, D. K. Thomas, J. C. Conrad, and R. Krishnamoorti, "Diffusive dynamics of nanoparticles in arrays of nanoposts," ACS Nano **7**, 5122–5130 (2013).

[95] Fuchs, T., W. Richtering, W. Burchard, K. Kajiwara, and S. Kitamura, "Gel point in physical gels: Rheology and light scattering from thermoreversibly gelling schizophyllan," Polym. Gels Networks **5**, 541–559 (1998).

[96] Krall, A. H., Z. Huang, and D. A. Weitz, "Dynamics of density fluctuations in colloidal gels," Phys. A: Statistical Mech. Appl. **235**, 19–33 (1997).

[97] Cho, J. H., R. Cerbino, and I. Bischofberger, "Emergence of multiscale dynamics in colloidal gels," Phys. Rev. Lett. **124**, 088005 (2020).

[98] Liu, C., J. He, E. Ruymbeke, R. Keunings, and C. Bailly, "Evaluation of different methods for the determination of the plateau modulus and the entanglement molecular weight," Polymer **47**, 4461–4479 (2006).

[99] Rendell, R. W., K. L. Ngai, and G. B. McKenna, "Molecular weight and concentration dependences of the terminal relaxation time and viscosity of entangled polymer solutions," Macromolecules **20**, 2250–2256 (1987).

[100] Milner, S. T., "Unified entanglement scaling for flexible, semiflexible, and stiff polymer melts and solutions," Macromolecules **53**, 1314–1325 (2020).

[101] Schmidt, C. F., M. Baermann, G. Isenberg, and E. Sackmann, "Chain dynamics, mesh size, and diffusive transport in networks of polymerized actin: A quasielastic light scattering and microfluorescence study," Macromolecules **22**, 3638–3649 (1989).

[102] Gardel, M. L., M. T. Valentine, J. C. Crocker, A. R. Bausch, and D. A. Weitz, "Microrheology of entangled F-actin solutions," Phys. Rev. Lett. **91**, 158302 (2003).

[103] Shin, J. H., M. L. Gardel, L. Mahadevan, P. Matsudaira, and D. A. Weitz, "Relating microstructure to rheology of a bundled and cross-linked F-actin network in vitro," Proc. Natl. Acad. Sci. U.S.A. **101**, 9636–9641 (2004).

[104] Smrek, J., and A. Y. Grosberg, "Minimal surfaces on unconcatenated polymer rings in melt," ACS Macro Lett. **5**, 750–754 (2016).

[105] Chapman, C. D., and R. M. Robertson-Anderson, "Nonlinear microrheology reveals entanglement-driven molecular-level viscoelasticity of concentrated DNA," Phys. Rev. Lett. **113**, 098303 (2014).

[106] Al-Hadithi, T. S. R., H. A. Barnes, and K. Walters, "The relationship between the linear (oscillatory) and nonlinear (steady-state) flow properties of a series of polymer and colloidal systems," Colloid Polym. Sci. **270**, 40–46 (1992).

[107] Cox, W. P., and E. H. Merz, "Correlation of dynamic and steady flow viscosities," J. Polym. Sci. **28**, 619–622 (1958).

[108] Graessley, W. W., *The Entanglement Concept in Polymer Rheology* (Springer, Berlin, 1974), pp. 1–179.

[109] Kröger, M., and S. Hess, "Rheological evidence for a dynamical crossover in polymer melts via nonequilibrium molecular dynamics," Phys. Rev. Lett. **85**, 1128–1131 (2000).

[110] Cerbino, R., and V. Trappe, "Differential dynamic microscopy: Probing wave vector dependent dynamics with a microscope," Phys. Rev. Lett. **100**, 188102 (2008).

[111] Giavazzi, F., and R. Cerbino, "Digital Fourier microscopy for soft matter dynamics," J. Opt. **16**, 083001 (2014).

[112] Ricketts, S. N., M. L. Francis, L. Farhadi, M. J. Rust, M. Das, J. L. Ross, and R. M. Robertson-Anderson, "Varying crosslinking motifs drive the mesoscale mechanics of actin-microtubule composites," Sci. Rep. **9**, 12831 (2019).

[113] Regan, K., D. Wulstein, H. Rasmussen, R. McGorty, and R. M. Robertson-Anderson, "Bridging the spatiotemporal scales of macromolecular transport in crowded biomimetic systems," Soft Matter **15**, 1200–1209 (2019).

[114] Falzone, T. T., and R. M. Robertson-Anderson, "Active entanglement-tracking microrheology directly couples macromolecular deformations to nonlinear microscale force response of entangled actin," ACS Macro Lett. **4**, 1194–1199 (2015).

[115] Anderson, S. J., J. Garamella, S. Adalbert, R. J. McGorty, and R. M. Robertson-Anderson, "Subtle changes in crosslinking drive diverse anomalous transport characteristics in actin–microtubule networks," Soft Matter **17**, 4375–4385 (2021).

[116] Garamella, J., K. Regan, G. Aguirre, R. J. McGorty, and R. M. Robertson-Anderson, "Anomalous and heterogeneous DNA transport in biomimetic cytoskeleton networks," Soft Matter **16**, 6344–6353 (2020).

[117] Anderson, S. J., C. Matsuda, J. Garamella, K. R. Peddireddy, R. M. Robertson-Anderson, and R. McGorty, "Filament rigidity vies with mesh size in determining anomalous diffusion in cytoskeleton," Biomacromolecules **20**, 4380–4388 (2019). .

[118] Wong, I. Y., M. L. Gardel, D. R. Reichman, E. R. Weeks, M. T. Valentine, A. R. Bausch, and D. A. Weitz, "Anomalous diffusion probes microstructure dynamics of entangled F-actin networks," Phys. Rev. Lett. **92**, 178101 (2004).

[119] Hess, S., "Fokker-Planck-Equation approach to flow alignment in liquid crystals," Z. Nat. A **31**, 1034–1037 (1976).

[120] See supplementary material at https://www.scitation.org/doi/suppl/10.1122/8.0000447 for the following figures: gel electrophoresis of linear and ring DNA solutions (Fig. S1); sample images of labeled DNA from time-series recorded before and after bulk rheology measurements (Fig. S2); nominal entanglement lengths computed from the plateau modulus for DNA in DNA-dextran composites (Fig. S3); sample DDM intermediate scattering functions for DNA-dextran composites (Fig. S4); variations in the intermediate scattering function across different regions of interest (Fig. S5.); and van Hove distributions show non-Gaussianity indicative of heterogeneous transport at short timescales (Fig. S6).